MOLECULAR DIFFUSION AS MEASURED BY PULSED FIELD GRADIENT NUCLEAR MAGNETIC RESONANCE

A thesis presented in partial fulfilment
of the requirements for the degree
of Master of Science
in Chemistry at
Massey University

JEREMY SAMUEL DRUCE KISSOCK

1982

ABSTRACT

The work presented in this thesis may be conveniently divided into three sections.

Firstly the development of a Carr-Purcell-Meiboom-Gill pulse sequence for use in the pulsed field gradient experiment in order to examine diffusion over long diffusion times is described.

Secondly diffusion coefficients of both components of binary mixtures of methanol and benzene have been measured using pulsed field gradient fourier transform NMR. Results showed self-association to be dominant over AB association and a brief qualitative explanation of the reasons for this is given.

In the third section, which is the major part of this thesis, diffusion coefficients of water in the caesium perfluoro-octanoate, water system have been determined at various weight fractions and temperatures by pulsed field gradient NMR. The liquid crystalline phases occuring within the system are the isotropic micellar solution, the nematic amphiphilic mesophase and the smetic lamellar mesophase. Water was found to pass through the system in an unrestricted and virtually unhindered manner. These results were discussed in terms of the known structures of the phases and with respect to possible permeation mechanisms. No definite conclusion as to the permeation mechanism is possible. The limitations in the use of surfactants as membrane models is discussed.

ACKNOWLEDGEMENTS

I wish to thank my supervisor Dr. Kenneth Jolley for his constant encouragement and invaluable assistance and advice.

I am grateful also to Dr Paul Callaghan for his advice and assistance in the use of the NMR spectrometer, as well as to members of the chemistry department for their helpful comments and encouragement.

I thank the staff of the electronics workshop for their assistance and cooperation.

I am also most grateful to Janet Sayers and Lorraine Stewart for typing this thesis.

TABLE OF CONTENTS

SECTION THREE

APPENDICES

ABBREVIATIONS

A_∞ , A_τ	amplitudes of FID signal after 90° pulse at times $t = \infty$ and $t = \tau$ in a 180°, τ , 90° experiment
B	magnetic field
B_o	magnetic field (externally applied)
B_1	magnetic field from the radiofrequency pulse
$B_{eff.}$	an effective magnetic field, defined by equation 17
CsPFO	caesium perfluoro-octanoate
CPMG	Carr-Purcell-Meiboom-Gill
dc	direct current
D	diffusion coefficient
$D_\perp, D_{\|\|}$	components of D parallel and perpendicular to symmetry axis
E_A	activation energy
F I D	free induction decay
FT	Fourier transform
g_o	uniform and stationary field gradient
$g(\omega)$	absorption line shape, defined by equation [24]
G	magnetic field gradient
h	Planck's constant
$\hbar$	modfield Planck's constant, equal to $h/2\pi$
$\hat{\underline{i}}$	unit vector along the x axis
I	nuclear spin quantum number
IC	integrated circuit
$\hat{\underline{j}}$	unit vector along the y axis
k	Boltzmann constant
$\hat{\underline{k}}$	unit vector along the z axis
LiPFO	lithium perfluoro-octanoate
m_I	direction of vector components of nuclear spin angular moments
M	macroscopic magnetization vector
N_α , N_β	number of spins in the α and β energy states, defined by equation 6
NMR	nuclear magnetic resonance
O.D.	outer diameter
$\underline{P}$	nuclear angular momentum vector
PFG	pulsed field gradient

PFO	perfluoro-octanoate
r.f.	radiofrequency
R	gas constant
RMS	root mean square
t	time
t_1	delay time in applying the first field gradient pulse
t_2	equal to $2\tau-(t_1 + \Delta + \delta)$
T	Kelvin temperature
T_1	longitudinal or spin-lattice relaxation time
T_2	transverse or spin-spin relaxation time
U	energy
ΔU	separation between two energy levels
x,y,z	cartesian coordinate system axis
γ	magnetogyric ratio
δ	duration of field gradient pulses
Δ	separation between two field gradient pulses
θ	angle
μ	nuclear magnetic moment
ν_o, ω_o	resonance frequencies
σ	screening constant
ω	angular frequency
τ	time between pulses in a pulse sequence

SECTION ONE

NUCLEAR MAGNETIC RESONANCE THEORY

A. Quantum Mechanical Treatment (1,2)

1.1 N.M.R. Energy Levels

Most nuclei behave as though they possess spin angular momentum ($\underline{P}$). The magnitude of $\underline{P}$ is given by :

$$P = \hbar\sqrt{I(I+1)}$$

and its direction by m_I which are the components of $\underline{P}$ along a reference direction. I is the quantum number for nuclear spin which can have half integral values and

$$m_I = +I, +I-1, \ldots, -I.$$

e.g. ^1H ... $I = 1/2$ (diagram 1)

magnitude of $P = \hbar\sqrt{I(I+1)} = \sqrt{3/4}\,\hbar$

and $m_I = +1/2$ or $-1/2$

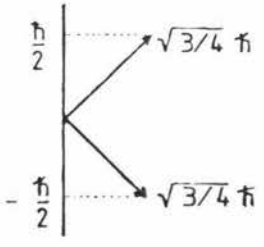

diagram 1

The spin and charge of the nucleus confers a magnetic moment(μ):

$$\underline{\mu} = \gamma\hbar\underline{I}$$

or $$\mu_z = \gamma\hbar\, m_I$$

$$= \gamma P_z$$

where γ is the magnetogyric ratio, the ratio of magnetic moment to angular momentum, and is a constant for a given nucleus.

The following discussion will be mainly confined to the I = 1/2 nucleus since this thesis was primarily concerned with ^{1}H.

If a steady magnetic field ($\underline{B}$) is applied to the nucleus there is an interaction between the field and the magnetic moment which may be represented by :

$$U = -\underline{\mu} \cdot \underline{B}$$

(where U is the energy of the interaction). If the direction of the magnetic field is in the z direction the interaction may be rewritten :

$$U = -\mu_z \cdot B = -\gamma \hbar m_I B \qquad [4]$$

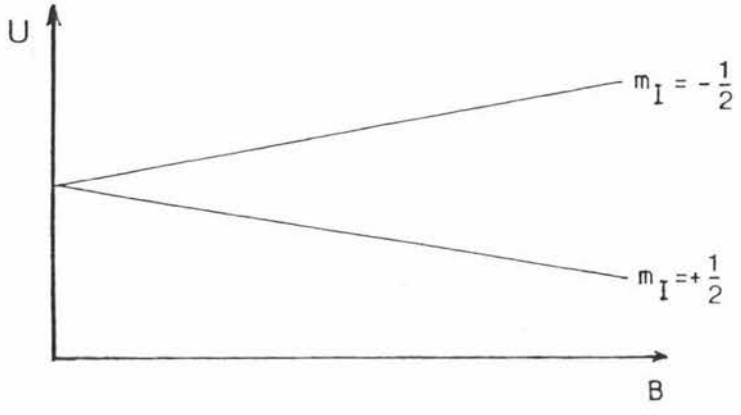

diagram 2

The selection rule for the transition between energy levels is $\Delta m = \pm 1$.

$$\Delta U = h\nu = \gamma \hbar B$$

$$\text{Therefore} \quad \nu = \gamma B / 2\pi \qquad [5]$$

where ν is the frequency of radiation needed to bring about transition. Note that the energy separation depends upon the strength of the magnetic field (diagram 2).

The allowed values that the spins will take will be in a Boltzmann

distribution. If there are N_α spins in the lower state and N_β spins in the upper state; the ratio of α to β spins is:

$$\frac{N_\beta}{N_\alpha} = \exp(-\gamma\hbar B/kT) \qquad [6]$$

For example: $B_o = 1.4$ Tesla $\qquad T = 300$ K

for a ^1H nucleus.

$$\frac{N_\beta}{N_\alpha} = 0.9999905$$

That is, only a very small (but detectable) excess of spins exist in the lower, α , state.

1.2 The Chemical Shift

The resonance lines from liquids are exceedingly narrow and consequently very small interactions can be detected. The two types of interaction which are important are the nuclear zeeman interaction and nuclear spin-spin coupling. The surrounding electrons in a molecule produce shielding effects which change the zeeman term from

$$U = -\gamma\hbar m_I B$$

to

$$U = -\gamma\hbar m_I (1-\sigma)B \qquad [7]$$

This is because the actual field at the nucleus is the sum of two magnetic fields; B, the applied field and $-\sigma B$, the local field at the nucleus arising from the induced electronic currents.

B. Classical Treatment (1,2,3)

1.3 Precession

It can be shown by classical mechanics that the torque exerted on a magnetic moment by a magnetic field inclined at an angle θ relative to the moment causes the magnetic moment to precess about the direction of the field (diagram 3).

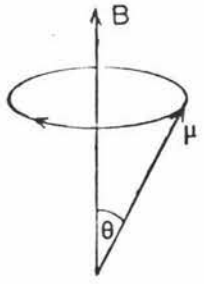

diagram 3

The frequency of precession is known as the Larmour frequency.

$$\frac{d\underline{P}}{dt} = \underline{\mu} \times \underline{B}$$

since $\underline{\mu} = \gamma \underline{P}$

$$\frac{d\underline{\mu}}{dt} = \underline{\mu} \times (\gamma \underline{B}) \qquad [8]$$

If $B = B_o \hat{\underline{k}}$, where $\hat{\underline{k}}$ is the z unit vector, then the spin will precess at an angular frequency where

$$\omega_o = -\gamma B_o \qquad [9]$$

1.4 The Rotating Frame of Reference

In the treatment of pulse methods it is usually simpler to refer the motion of magnetism to a coordinate system that rotates about B_o in the same direction which the nuclear moments precess , rather than the fixed coordinate system of the laboratory (diagram 4).

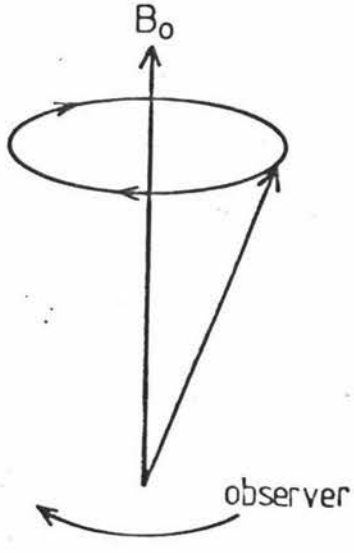

diagram 4

If $\underline{M}$ is the vector sum of all the μ's (diagram 5), then by summing equation 8 over all μ the following relation is obtained:

$$\frac{d\underline{M}}{dt} = \gamma \underline{M} \times \underline{B} \qquad [10]$$

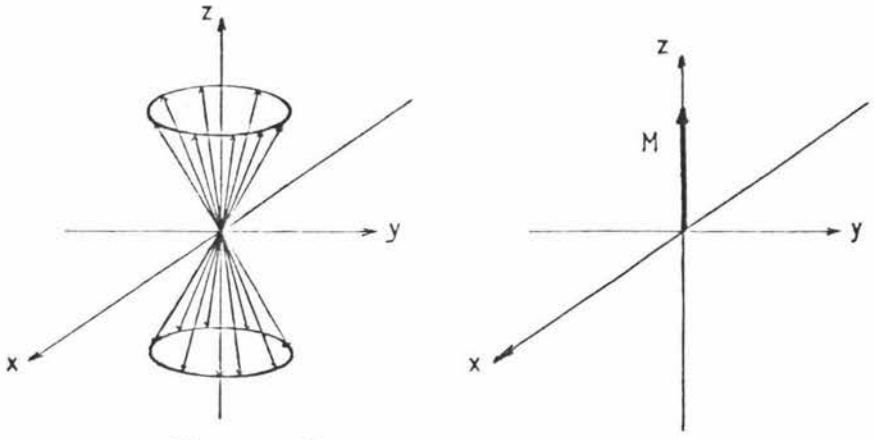

diagram 5

M can be considered in terms of components along the three cartesian axes:

$$\underline{M} = M_x \hat{\underline{i}} + M_y \hat{\underline{j}} + M_z \hat{\underline{k}} \qquad [11]$$

Therefore

$$\frac{d\underline{M}}{dt} = \left(\frac{\partial M_x \hat{\underline{i}}}{\partial t} + \frac{\partial M_y \hat{\underline{j}}}{\partial t} + \frac{\partial M_z \hat{\underline{k}}}{\partial t} \right) + \left(\frac{M_z \partial \hat{\underline{i}}}{\partial t} + \frac{M_y \partial \hat{\underline{j}}}{\partial t} + \frac{M_z \partial \hat{\underline{k}}}{\partial t} \right) \qquad [12]$$

$\hat{\underline{i}}$, $\hat{\underline{j}}$, $\hat{\underline{k}}$ are unit vectors and therefore their time derivatives can only rotate the vectors:

$$\frac{\partial \hat{\underline{i}}}{\partial t} = \omega \times \hat{\underline{i}} \, , \quad \frac{\partial \hat{\underline{i}}_n}{\partial t} = \omega \times \hat{\underline{j}} \, , \quad \frac{\partial \hat{\underline{k}}}{\partial t} = \omega \times \hat{\underline{k}} \qquad [13]$$

The speed and direction of the unit vectors are defined by the same ω; hence equation [12] becomes:

$$\left(\frac{d\underline{M}}{dt} \right)_{\text{fixed}} = \frac{\partial \underline{M}}{\partial t} + \omega \times (M_x \hat{\underline{i}} + M_y \hat{\underline{j}} + M_z \hat{\underline{k}})$$

$$= \left(\frac{\partial \underline{M}}{\partial t}\right)_{rot} + \omega \times \underline{M} \qquad [14]$$

From equation [10]

$$\left(\frac{d\underline{M}}{dt}\right)_{fixed} = \gamma \underline{M} \times \underline{B}$$

and from equation [14]

$$\left(\frac{d\underline{M}}{dt}\right)_{rot} = \gamma \underline{M} \times \underline{B} - \omega \times \underline{M}$$

rearranging:

$$\left(\frac{d\underline{M}}{dt}\right)_{rot} = \gamma \underline{M} \times \underline{B} + \gamma \underline{M} \times \frac{\omega}{\gamma}$$

$$= \gamma \underline{M} \times \left(\underline{B} + \frac{\omega}{\gamma}\right) \qquad [15]$$

The term ω/γ can be considered as a fictitious field that arises from the effect of the rotation. Alternatively equation [15] may be rewritten :

$$\left(\frac{d\underline{M}}{dt}\right)_{rot} = \gamma \underline{M} \times \underline{B}_{eff}. \qquad [16]$$

where $\underline{B}_{eff}$ is the effective field, that is :

$$\underline{B}_{eff} = \underline{B} + \omega/\gamma \qquad [17]$$

In the rotating frame, therefore, $\underline{M}$ precesses about $\underline{B}_{eff}$. If in addition to $\underline{B}$ a radiofrequency field B_1 is applied at right angles, then in the rotating frame at the Larmor frequency

$$\underline{B}_{eff} = B_o + \omega_o/\gamma + B_1$$

and the fictitious field exactly cancels B_o along the z axis and leaves only B_1 in the xy plane to interact with M. However in most situations B_1 and the rotating frame move at a frequency different from the resonance frequency as so the relation depicted in diagram 6 occurs where the fictitious field does not cancel B_o and leaves a component of the effective field in the z' direction. Mathematically the result is:

$$|B_{eff}| = [(B_o - \omega/\gamma)^2 + B_1^2]^{\frac{1}{2}}$$

$$= (1/\gamma)[(\omega_o - \omega)^2 + (\gamma B_1)^2]^{\frac{1}{2}}$$

Providing $B_1 \gg (\omega_o - \omega)$ then $B_{eff} = B_1$

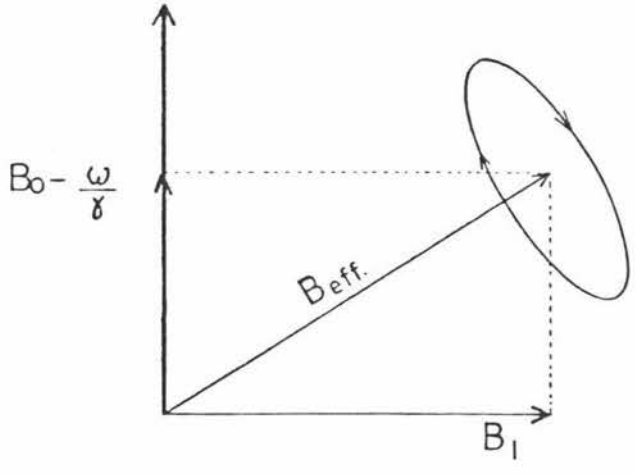

diagram 6

1.5 The Bloch Equations

Bloch et al. (4) found that the motion of the macroscopic magnetization in the presence of a magnetic field could be explained in terms of differential equations.

The vector product of equation [10] may be expanded in terms of components along the three cartesian axes and the unit vectors along these axes.

$$\underline{M} \times \underline{B} = (\hat{\underline{i}} M_x + \hat{\underline{j}} M_y + \hat{\underline{k}} M_z) \times (\hat{\underline{i}} B_x + \hat{\underline{j}} B_y + \hat{\underline{k}} B_z)$$

$$= \hat{\underline{k}} M_x B_y - \hat{\underline{j}} M_x B_z - \hat{\underline{k}} M_y B_x + \hat{\underline{i}} M_y B_z$$

$$+ \hat{\underline{j}} M_z B_x - \hat{\underline{i}} M_z B_y$$

$$\Longleftrightarrow \quad \underline{M} \times \underline{B} = (M_y B_z - M_z B_y) \hat{\underline{i}} + (M_z B_x - M_x B_z) \hat{\underline{j}}$$

$$+ (M_x B_y - M_y B_x) \hat{\underline{k}} \qquad [18]$$

In general this equation consists of both the static applied field, B_o , and the magnetic vector of the r.f. field , B_1 . The radio frequency field can be thought of as two vector fields rotating in opposite directions (diagram 7).

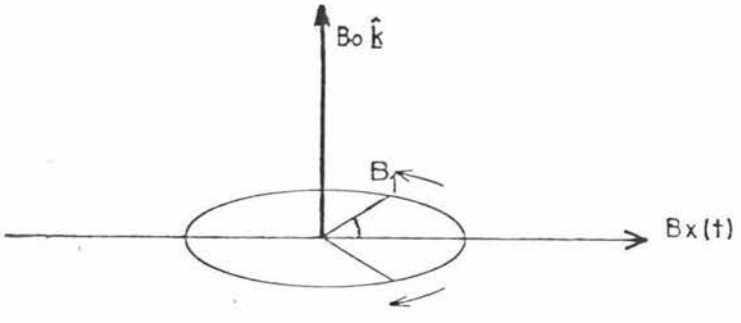

diagram 7

$$\underline{B}\,(t) = B_x(t)\,\hat{\underline{i}} \quad = 2B_1 \cos\omega t\,\hat{\underline{i}}$$

$$= B_1[\,\hat{\underline{i}} \cos\omega t + \hat{\underline{j}} \sin\omega t\,] + B_1\,[\,\hat{\underline{i}} \cos\omega t - \hat{\underline{j}} \sin\omega t\,]$$

[19]

The only field that needs to be considered is the one that rotates in the same direction as the nuclear moments , therefore

$$B_1(t) = B_1\,[\hat{\underline{i}} \cos\omega t - \hat{\underline{j}} \sin\omega t\,] \qquad [20]$$

Hence
$$\frac{dM_x}{dt} = \gamma B_o M_y + \gamma M_z B_1 \sin \omega t \qquad [20]a$$

$$\frac{dM_y}{dt} = -\gamma B_o M_x + \gamma M_z B_1 \cos \omega t \qquad [20]b$$

$$\frac{dM_z}{dt} = 0 - \gamma M_x B_1 \sin \omega t - \gamma M_y B_1 \cos \omega t \qquad [20]c$$

These equations are not complete since they do not account for the relaxation that must occur following a r.f. pulse. Decay to equilibrium occurs via a first order process with M_x and M_y decaying to zero and M_z to the equilibrium value of M_o. Hence:

$$\frac{dM_z}{dt} = -\gamma M_x B_1 \sin \omega t - \gamma M_y B_1 \cos \omega t + \frac{M_o - M_z}{T_1} \qquad [21]$$

$$\frac{dM_x}{dt} = \gamma B_o M_y + \gamma M_z B_1 \sin \omega t - \frac{M_x}{T_2} \qquad [22]$$

$$\frac{dM_y}{dt} = -\gamma B_o M_x + \gamma M_z B_1 \cos \omega t - \frac{M_y}{T_2} \qquad [23]$$

These are the Bloch equations. T_1 and T_2 are the longitudinal and transverse relaxation times respectively since they are time constants for decay along and perpendicular to B_o.

There are two methods for observing nuclear magnetic resonance; the continuous wave technique and pulse methods. The continuous wave method consists of sweeping the frequency of the r.f. field applied to a sample in a fixed magnetic field (or sweeping B_o with a fixed r.f. field). The signal is observed as an absorption line. The pulse method makes use of short bursts of r.f. power at a discrete frequency with the observation of the nuclear spin system being made after the r.f. field is turned off. Pulse methods are the superior being quicker and more versatile.

In the continuous wave experiment B_1 is small and the sweep rate is slow.

i.e. $\frac{dM}{dt}\, x,y,z = 0$

Under these conditions the Bloch equations can be solved to give the line shape for the absorption signal g(w). The line shape is Lorentzian and is given by (2):

$$g(w) = \frac{K\,T_2}{1 + T_2^2\,(\omega_o - \omega)^2} \qquad [24]$$

K is a constant.

1.6 Pulsed Nuclear Magnetic Resonance

If the r.f. field , at the Lamour frequency , is turned on for a time t , then viewed in the rotating frame the effective field becomes aligned with the x axis and the magnetization vector will begin to tip towards this axis (diagram 8).

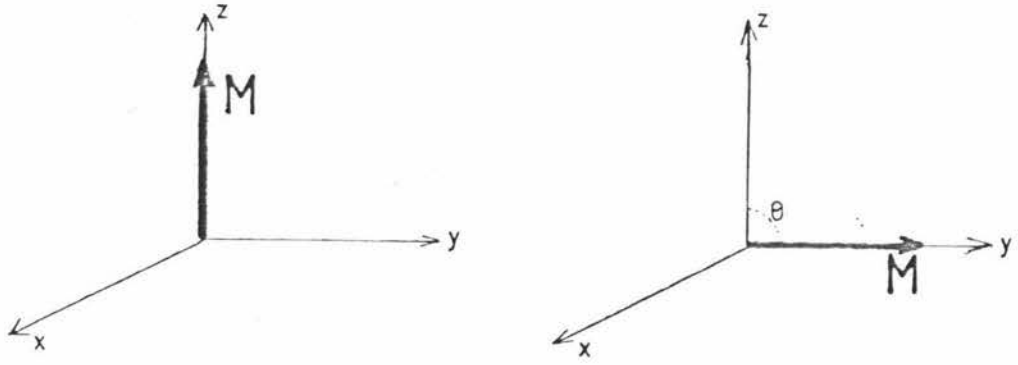

diagram 8

$$\theta = \omega_{eff}\, t = \gamma \underline{B}_{eff}\, t = \gamma B_1\, t$$

$$\text{i.e.} \quad t = \frac{\theta}{\gamma B_1} \qquad [25]$$

When B_1 is off the magnetization will return to its equilibrium value along B_o.

Evolution of M_z following a 180^o pulse

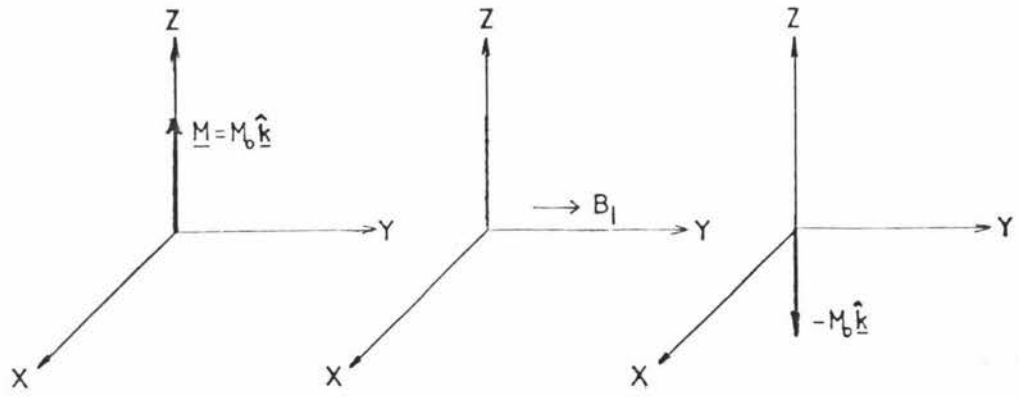

diagram 9

The evolution starts immediately following the 90^o pulse.

$$M_z(t=0) = -M_o$$

$$M_x(0) = 0$$

$$M_y(0) = 0$$

using the Bloch equations :

$$\frac{dM_z}{dt} = \frac{M_o - M_z}{T_1}$$

$$\int_{M=Mo}^{M_z} \frac{dM_z}{M - M_z} = \int_{t=o}^{t} \frac{dt}{T_1}$$

$$M_z(t) = M_o\left(1 - 2\exp(-\frac{t}{T_1}\right) \qquad \text{(diagram 10)} \qquad [26]$$

Evolution of M_x , M_y and M_z following a 90^o pulse (diagram 12).

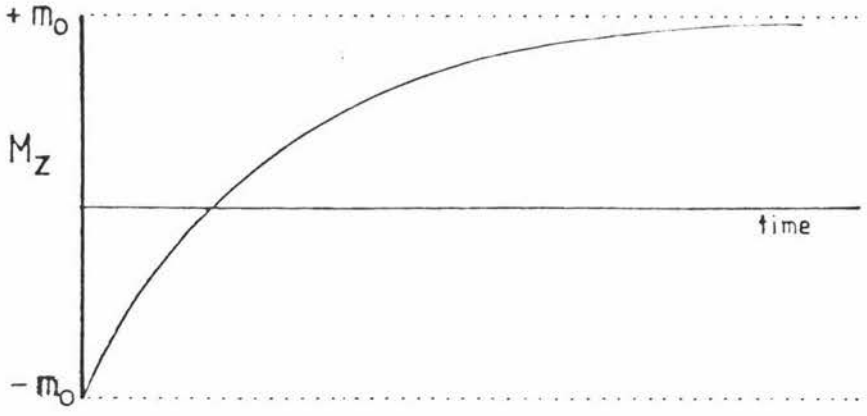

diagram 10

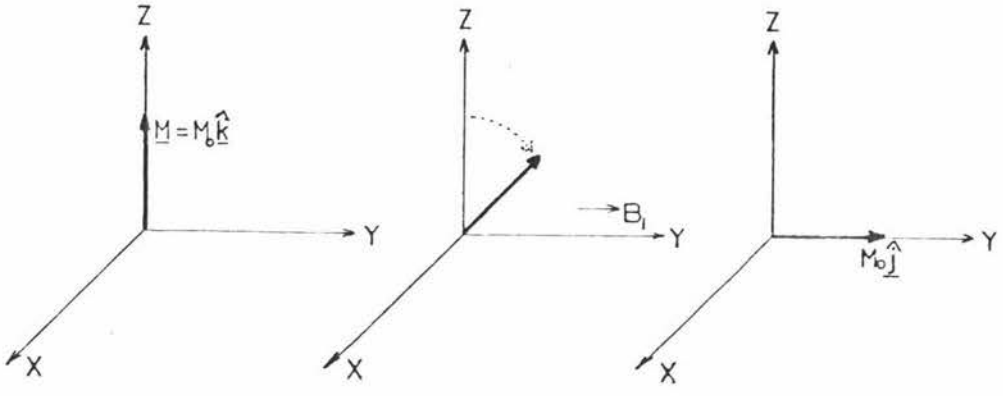

diagram 11

$$M_z(0) = 0 \ , \ M_x(0) = 0 \ , \ M_y(0) = 0$$

Using the Bloch equations :

(a) Evolution of M_z

$$\int_{M=0}^{M_z} \frac{dM}{M_o - M_z} = \int_{t=0}^{t} \frac{dt}{T_1}$$

$$\Rightarrow \quad - \ln(M_o - M_z) + \ln M_o = t/T_1$$

$$\Longleftrightarrow \quad M_z(t) = M_o(1 - \exp(-t/T_1)) \qquad [27]$$

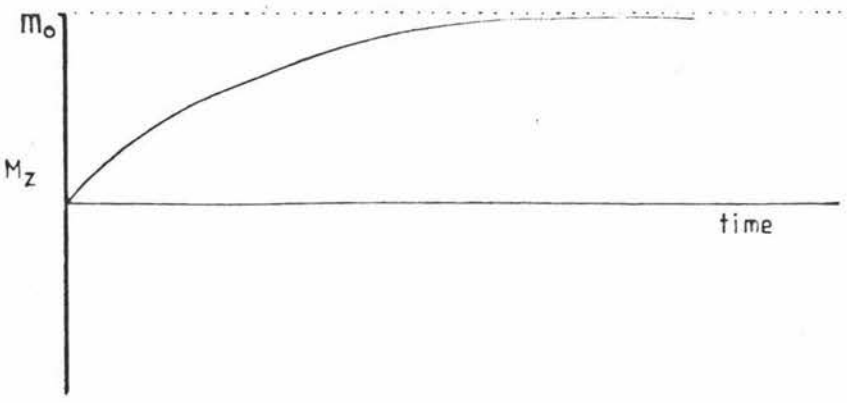

Diagram 12

(b) Evolution of M_x

$$\frac{dM_x}{dt} = \gamma M_y B_o - \frac{M_x}{T_2}$$

$$\frac{d^2M_x}{dt^2} = \gamma B_o \frac{dM_y}{dt} - \frac{dM_x}{dt}\frac{1}{T_2}$$

Substituting firstly for dM_y/dt from equation [20]b and secondly for M_y from equation [20]a gives a second order differential equation which has the solution:

$$M_x(t) = M_o \exp(-t/T_2) \sin \gamma B_o t$$
$$= M_o \exp(-t/T_2) \sin 2\pi \nu_o t$$

The resulting spectrum is known as a free induction decay or FID:

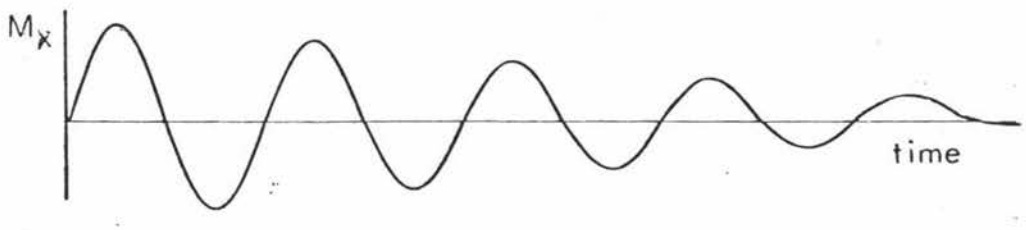

diagram 13

Similarly it can be shown that :

$$M_y(t) = M_o \exp(-t/T_2) \cos 2\pi \nu_o t \qquad [28]$$

1.7 Measurement of Relaxation Times

(a) T_1 by Inversion Recovery

This is the most common procedure used. It consists of varying τ in the 180° - τ - 90° pulse sequence. The 180° pulse takes $\underline{M}$ out of thermal equilibrium, but still along the z axis. After a time τ a 90° pulse takes the remaining M_z into the transverse plane so that its magnitude can be detected in the transverse detector coils. From equation [26] :

$$\ln (A_\infty - A_\tau) = \ln 2A_\infty - \tau/T_1 \qquad [29]$$

A_τ is the initial amplitude of the F.I.D. following the 90° pulse at a time τ , and A_∞ is the limiting value for a very long interval between the 180° and 90° pulses. T_1 is determined from the slope of a plot of ln ($A_\infty - A_\tau$) versus τ.

(b) Measurement of T_2

If B_o was perfectly homogeneous then one could determine T_2 simply by observing the decay of $M_{x,y}$ after a 90° pulse. Because B_o is not perfectly homogeneous some of the nuclear magnets precess faster than ω_o and some slower. Dephasing of spins therefore occurs , lowering $M_{x,y}$ and shortening the observed T_2 .

Because of this problem T_2 is commonly measured by the modified Hahn spin-echo method (5). This method greatly reduces the effect of

field inhomogeneities. It consists of the application of a $90^{o}/x$ — τ — $180^{o}/y$ pulse sequence and the observation at a time 2τ of the free induction echo. The full Hahn expression is:

$$A(2\tau) \propto \exp\left[\frac{-2\tau}{T_2} - \frac{2}{3}\gamma^2 G^2 D \tau^3\right] \qquad [30]$$

This equation shows that the echo amplitude does not decay in a simple exponential fashion. The spin - echo method is limited in its range of applicability due to the effect of molecular diffusion. If diffusion causes nuclei to move from one part of an inhomogeneous field to another the echo amplitude is reduced. The effect of diffusion is particularly pronounced for large values of τ and thus may affect measurements of long T_2.

Carr-Purcell-Meiboom-Gill method for measuring T_2 (CPMG) (6,7)

Because of the limited range in applicability of the spin-echo method a CPMG sequence may often be used. The pulse sequence used in this study consists of a $90^{o}/x$ — τ — $180^{o}/y$ — 2τ — $180^{o}/_{-y}$ — 2τ — .... sequence with observation of echo heights at 2τ, 4τ, 6τ, 8τ, etc. There are two distinct advantages of the CPMG sequence. Firstly; there is a considerable saving in time, for a train of n echoes may be obtained in a single sequence. Secondly; the effect of diffusion may be virtually eliminated by making τ short since it is only during a time 2τ that diffusion is effective in reducing the amplitude of an echo. For the CPMG sequence:

$$A(t) \propto \exp\left[\frac{-t}{T_2} - \frac{1}{3}\gamma^2 G^2 D \tau^2 t\right] \qquad [31]$$

Note the τ^2 term of the CPMG method compared with the τ^3 term of the spin-echo method. The change of phase of the 180^{o} pulses from the initial 90^{o} pulse (from being applied along the x axis, to the y axis) and the change in direction of application of the r.f. pulses (y, -y, y etc.) reduces the cumulative error from the not exactly accurate pulse time, t_p.

1.8 Fourier Analysis and Fourier Transformation

It is often useful to sort out what frequencies are present in a complex waveform and to determine the intensity of each of the frequencies present. By using the principles of fourier analysis it is possible to transform from the F.I.D. to the corresponding frequencies. A function A(t) can usually be expressed as an infinite series of sines and cosines :

$$A(t) = \sum_{n=0}^{\infty} A_n \cos(n\pi/T)t + \sum_{n=1}^{\infty} B_n \sin(n\pi/T)t \qquad [32]$$

(A_n and B_n are variable constants)
The r.f. signal emitted by the sample induces an oscillating e.m.f., $\delta(t)$, in the probe detector coil :

$$\delta(t) = \delta_o \exp(-t/T_2) \sin 2\nu_o \pi t \qquad [33]$$

A phase sensitive detector is used to shift the signal to the audio range :

$$\delta(t) = \delta_o \exp(-t/T_2)\{\alpha \sin 2\pi\Delta\nu t + \beta \cos 2\pi\Delta\nu t\} \qquad [34]$$

where $\Delta\nu = \nu_o - \nu_{ref}$ and α and β depend upon the phase setting of the r.f. reference.

$$\alpha^2 + \beta^2 = 1 \qquad [35]$$

(a) Sine Transform

$$F^S(\nu) = \int_{t=o}^{\infty} \delta(t) \sin 2\pi\nu t \, dt$$

$$= \delta_o \alpha \int_{t=o}^{\infty} \exp(-t/T_2) \sin 2\pi\Delta\nu t \sin 2\pi\nu t \, dt$$

$$+ \delta_o \beta \int_{t=o}^{\infty} \exp(-t/T_2) \cos 2\pi\Delta\nu t \sin 2\pi\nu t \, dt$$

$$= \frac{\delta_o \alpha}{2} \left\{ \frac{(1/T_2)}{(1/T_2)^2 + (2\pi(\nu - \Delta\nu))^2} - \frac{(1/T_2)}{(1/T_2)^2 + (2\pi(\nu + \Delta\nu))^2} \right\}$$

$$+ \frac{\delta_o \beta}{2} \left\{ \frac{2\pi(\nu + \Delta\nu)}{(1/T_2)^2 + (2\pi(\nu - \Delta\nu))^2} + \frac{2\pi(\nu - \Delta\nu)}{(1/T_2)^2 + (2\pi(\nu - \Delta\nu))^2} \right\}$$

[36]

(b) Cosine Transformation

$$F^c(\nu) = \int_{t=0}^{\infty} \delta(t) \cos 2\pi\nu t \; dt$$

$$= \frac{\delta_o \alpha}{2} \left\{ \frac{2\pi(\nu + \Delta\nu)}{(1/T_2)^2 + (2\pi(\nu + \Delta\nu))^2} - \frac{2\pi(\nu - \Delta\nu)}{(1/T_2)^2 + (2\pi(\nu - \Delta\nu))^2} \right\}$$

$$+ \frac{\delta_o \beta}{2} \left\{ \frac{(1/T_2)}{(1/T_2)^2 + (2\pi(\nu - \Delta\nu))^2} + \frac{1/T_2}{(1/T_2)^2 + (2\pi(\nu + \Delta\nu))^2} \right\}$$

[37]

Only the positive frequencies are displayed. To obtain an absorption spectrum it may be necessary to admix the positive frequency parts of $F^s(\nu)$ and $F^c(\nu)$ in the proportions

$$\alpha F^s(\nu) + \beta F^c(\nu)$$

The result is :

$$A = \frac{\delta_o}{2} (\alpha^2 + \beta^2) \left\{ \frac{(1/T_2)}{(1/T_2)^2 + (2\pi(\nu - \Delta\nu))^2} \right\} \qquad [38]$$

Where A is the absoption peak height. The shape of the curve is a Lorentzian curve :

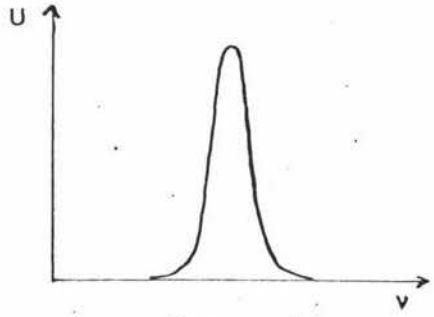

diagram 14

The frequency width at half the maximum peak height equals $1/\pi T_2$, therefore T_2 is measureable from the absorption signal. This method will be disadvantageous if either :

(i) Broadening from magnetic field inhomogeneities occurs.

(ii) There is a broadening due to overlapping peaks of similar chemical shift.

1.9 Definition of the Diffusion Coefficient

Molecular migration in condensed phases may be treated as point to point jumps of the elementary particles governed by a rate constant (8).

Consider the simple case of a system with molecules which are sufficiently alike so that the whole may be thought of as forming a more or less perfect lattice.

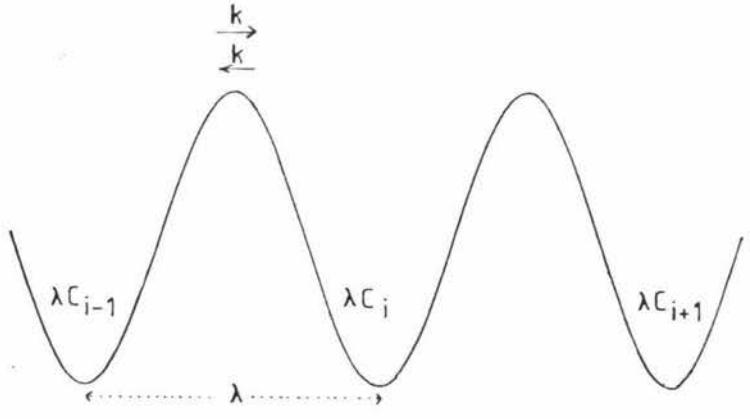

diagram 15

If C_i is the concentration per cubic centimeter at the i^{th} position , then the amount of material in a volume with a cross section of one square centimeter and length λ is λC_i (diagram 15). Let K represent the number of times per second a molecule jumps , and Q be the amount of C passing per second through a square centimeter of surface , then :

$$Q = K \lambda C_i - K \lambda C_{i+1} \qquad [39]$$

The concentration gradient between the i^{th} and the $(i + 1)^{th}$ position is :

$$\frac{dc}{dx} = \frac{C_{i+1} - C_i}{\lambda} \qquad [40]$$

Thus $$Q = K\lambda(C_i + C_{i+1}) = -K\lambda^2\frac{(C_{i+1} - C_i)}{\lambda} \qquad [41]$$

$$= -K\lambda^2\frac{dC}{dx}$$

This is Fick's First Law , normally written as:

$$Q = -D\,\frac{dC}{dx} \qquad [42]$$

where $D = K\lambda^2$
i.e. D has dimensions L^2T^{-1}

1.10 Methods of Measurement of Diffusion Rates

(1) Steady Gradient Technique

The full modified Hahn spin-echo equation is:

$$A(2\tau) = K\exp[-2\tau/T_2 - 2/3\ \gamma^2G^2D\tau^3] \qquad [30]$$

where Kis a constant. D can be measured by setting up an experiment to eliminate the first term of this sequence $(-2\tau/T_2)$, i.e. by keeping τ constant and varying G. The result is :

$$\frac{A_G}{A_o} = \exp\left(-\frac{2}{3}\gamma^2G^2D\tau^3\right) \qquad [43]$$

In principle D can be measured over a wide range but in practice there are limitations :

(a) It is extremely difficult to achieve τ values of

less than 50 μ sec.

(b) The magnetic field gradient , G , must be present at all times. As G becomes larger (in order to measure the slower diffusion rates) the width of the echo envolope becomes smaller. The consequences of this are

(i) the information available from the echo decreases ,

(ii) the band width of the detection system must be increased to observe the narrower echoes , lowering the signal / noise , and

(iii) with increasing linewidth the power output of the pulse transmitter will have to be increased to keep the r.f. field amplitude , B_1 , greater than the linewidth.

As a result of these problems the best results yet reported have a reproducibility of ±1% and an overall accuracy of ±2% (9). Furthermore , for systems in which the diffusion coefficient is spatially dependent it is desirable that the precise period of time during which diffusion is being observed be clearly defined. It is also desirable to make this time as short as possible.

(2) The Pulsed Field Gradient Method (10)

This consists of applying two magnetic field gradient pulses (G) of duration δ before and after the 180° pulse of the modified Hahn spin-echo method (diagram 16)

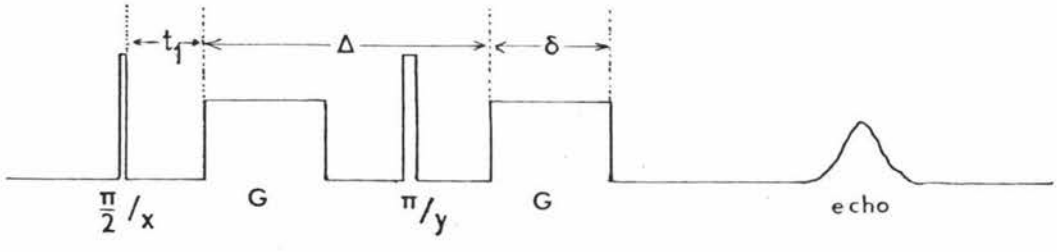

diagram 16

On application of the first gradient pulse there is a nearly instantaneous phase shift depending upon the location of each nucleus , a phase shift which records its position in the magnetic field.

This phase shift persists until it is inverted by the 180° pulse. A second phase shift occurs on application of the second gradient pulse. A nucleus which has had no net movement from its original position will refocus completely. Any motion that has occured results in incomplete refocusing. This , therefore , is a method for detecting net motion during a time interval $(\Delta - \delta/3)$. The effect on the echo amplitude by the application of the two gradient pulses is given by (10):

$$\ln[A(2\tau)/A(0)] = -\gamma^2 D \left\{ \frac{2}{3}\tau^3 g_o^2 + \delta^2(\Delta - \delta/3)\, G^2 \right.$$
$$\left. - \delta[(t_1^2 + t_2^2) + \delta(t_1 + t_2) + \frac{2}{3}\delta^2 - 2\tau^2]\, G.g_o \right\} \qquad [44]$$

where $t_2 = 2\tau - (t_1 + \Delta + \delta)$ and is the time between the end of the second gradient pulse and the peak of the echo , t_1 is the time at which the first gradient pulse occurs , and g_o is a uniform and stationary field gradient (due to field inhomogeneity). When G vanishes the result is the same as that obtained by the two pulse steady gradient spin-echo experiment , as expected. As g_o approaches zero (but not equal to zero since then there would be no loss of phase coherence) only the term in G^2 remains and the result is :

$$\ln[A(2\tau)/A(0)] = -\gamma^2 D G^2 \delta^2 \, (\Delta - \delta/3) \qquad [45]$$

When τ (Δ) , g_o or G are large then all three terms in the general equation may contribute. However if τ (or Δ) and g_o are small the diffusion coefficient can be determined by varying either G or Δ. Of the two variables , G is normally varied . In practice the direct determination of G is tedious and inaccurate. It is , therefore, usual to vary the current , I , supplied to the field gradient coils and to plot ln A(G)/A(0) versus $\gamma^2\delta^2(\Delta - \delta/3)\, I^2$ and determine the diffusion coefficient from the slope. This is possible for by the use of water at 25°C , where D is known , a conversion factor between I and G can be calculated.

1.11 Restricted Diffusion

$(\Delta - \delta/3)$ may be regarded as the effective diffusion time for the

experiment. The experimental mean square distance is thus : $\bar{z}^2 = 2D(\Delta - \delta/3)$ (11) . Since Δ is the order of a few milliseconds restricted diffusion effects may become visible . In practice $\bar{z}^2$ is required to be greater than (100 n m)^2 for any significant attenuation to be observed. If within a system there are no barriers or obstructions to the diffusing species , or if there are barriers they are separated by distances greater than the distances being experimentally observed , then unrestricted diffusion will be observed. Such diffusion may be regarded as being in three dimensions. This , however , is not always the case for in some systems layers or capillaries may exist with dimensions smaller than the experimental mean square distance that is being measured. If such a system is in layers , diffusion will be observed as being in two dimensions. If the system exists as capillaries , diffusion will occur in only one dimension. From the linearity , or non-linearity , of the $\ln[A(G)/A(0)]$ versus G^2 plot information as to whether the system is unrestricted , layered or in capillaries and the distance between the barriers may be obtained (21).

1.12 Inherent Errors and Their Solution Through a Modified CMPG Sequence (12)

As stated previously ; when g_o and τ (or Δ) are of significant magnitude then all three terms in the general equation of the pulsed field gradient technique may contribute. This problem may be overcome by using a modified CMPG sequence. A $\pi/2$ pulse is followed by a series of pairs of π_y and π_{-y} pulses , each π pulse following at a time 2τ after the previous one. Application of the first field gradient pulse is during an interval when the nuclei are dephasing. The second field gradient pulse is applied during a rephasing interval at a time Δ after the first one (diagram 17).

The result is (12) :

$$\ln[A(t_n)/A(0)] = -(t_n/T_2)$$

$$+ (-\gamma^2 D \left\{ 1/12\ n^2 g_o^2 t_n^3 + G^2\delta^2(\Delta - \tfrac{1}{3}\delta) \right.$$

$$\left. - G.g_o\delta[(t_1^2 + t_3^2) + \delta(t_1 + t_3) + \tfrac{2}{3}\delta^2 - 2\tau^2] \right\}) \qquad [46]$$

Where $A(t_n)$ is the amplitude of the echo that forms at the time t_n and $t_3 = \tau - t_1 - \delta$

Unless g_o is very large this can be approximated by:

$$\ln [A(t_n)/A(0)] = -\gamma^2 D G^2 \delta^2 (\Delta - \delta/3) \qquad [47]$$

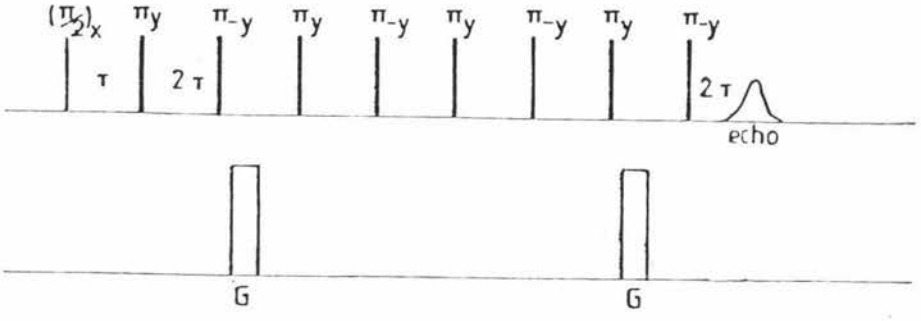

diagram 17

If only Δ is varied the effect of field inhomogeneity is removed and equation [47] becomes an equality.

SECTION TWO

EXPERIMENTAL PROCEDURES, METHODS AND EQUIPMENT

2.1 FX 60 Description

The spectrometer used was a JEOL FX60 60Mhz high resolution pulse spectrometer with Fourier transform capabilities. The magnetic field strength was approximately 1.4 tesla. To induce a 90^{o} change in orientation of the ^{1}H nuclear magnetization vector required a r.f. pulse of duration 26 μsec. The computer was a Texas Instruments 980A with 16K software storage capacity; 8K allocated to data manipulation and system control and 8K allocated to data storage. Entry into and manipulation of the computer software storage was by use of a light pen. The light pen is an input/output device used with a visual display unit. When pointed at a cathode ray tube it can sense whether or not a particular region is illuminated. This facility enables direct entry into the computer which allows quick and easy alteration of experimental parameters.

2.2 Diffusion Measurements

The diffusion measurements were made by interfacing the JEOL FX60 with a pulsed field gradient system designed and built by Callaghan et al. (13). The system used an external deuterium lock which in conjunction with signal averaging facilities enabled the more precise and accurate measurement of the diffusion coefficients. This ability is particularly important for the investigation of rates of diffusion of species in low concentrations. A set of $\partial B_z/\partial x$, $\partial B_z/\partial y$, $\partial B_z/\partial z$ homogeneity coils are in the probe. These coils give a residual gradient which is sufficiently small to resolve ^{1}H resonances $\sim$60hz apart enabling independent measurement of diffusion coefficients in some multicomponent systems. It is also useful for increasing signal/noise when working with dilute species. The magnitude of the field gradient pulses is varied by varying the current applied to the field gradient coils. Since the current, I, within a coil is proportional to the resultant magnetic field, the echo attenuation versus $I^2 \delta^2 (\Delta - \delta/3)$ may be plotted (see pg.21) and the diffusion coefficient may be obtained from the

slope.

The pulsed field gradient system consists, in part, of a pulse programmer. The function of the pulse programmer is to provide external switching of the current to the field gradient coils in accurately timed intervals (Δ , δ and t_1) in specific reference to the $90^{\circ}_{x}/180^{\circ}_{y}$ spin-echo pulses. The experimental parameters Δ , δ and t_1 are adjusted directly on BCD coded thumbwheel switches.

2.3 Temperature Control and Sample Space Geometry

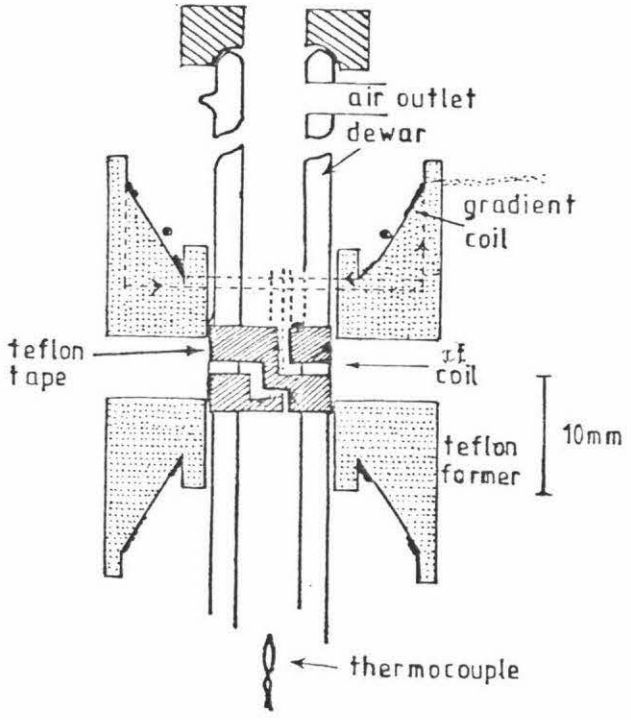

diagram 18

The temperature was controlled by using a copper-constantine thermocouple sensor in a conventional hot-air feedback system. Temperature was measured by a thermistor (quartz thermometer calibrated) placed in a NMR tube in the exact position the sample occupies. Temperature measurements were taken frequently to check for possible fluctuations. This involved removing the sample since it is not possible to simultaneously obtain spectra and temperature measurements. Temperature, when set, was accurate to $\sim 0.5^{\circ}C$ using a temperature control device (JES- V-T-3) made by J E O L.

2.4 Deuterium NMR Spectra

These were obtained by use of the ^{2}D lock channel. The lock is continuous wave and data is stored in the first 1K of the computer memory. The spectra can be displayed and analysed.

2.5 Inherent Errors in the use of a Modified Hahn Spin-Echo Sequence for Diffusion Experiments and the Solution of this Error by the use of a CPMG Sequence

As described earlier (pg. 22) advantages exist in using a CPMG pulse sequence as the basis for applying field gradient pulses during diffusion rate measurements. Over long diffusion distances this becomes desirable if accuracy is to be retained and over very large diffusion distances it becomes essential. Such large distances are often necessary when investigating restricted diffusion. The original field gradient pulse programmer could only accept two pulses from the spectrometer per echo sequence. After the first field gradient pulse was applied a variable amount of time (Δ) passed before application of the second rephasing field gradient pulse. If a CPMG sequence is occuring during this time interval more than two pulses will be received by the pulse programmer causing a malfunction and therefore excluding any CPMG diffusion experiment. Circuitry was built to overcome this problem. A diagramatic representation of the operation and circuitry are shown (diagrams 19 and 20). A general description of the circuit components follows (see appendix for additional information). The DN74LSOON integrated circuits (IC's) are NAND gates and the CD4017BC IC is a divide by ten counter being used here only in the '2' output. The SN74LS123N IC is a multivibrator which functions as a timing lock. Upon receiving a pulse at pin 10 of the multivibrator a change of state occurs at the Q and $\overline{Q}$ output terminals. This change of state exists for a time interval, dependent upon the resistor and capacitator values R_T and C_{ext}, and then returns back to the respective original state. The retrigger capability of the SN74L123N IC

made design considerably easier. Upon application of an additional pulse to the input terminal (pin 10) of the SN74L123N IC, during the timing interval, the timer is retriggered and timing is begun again without any change in state at the output. This retrigger capability simplified the generation of output pulses of long duration. The length of the output pulse is primarily a function of the external capacitor $C_{ext.}$ and resistor (R_T). The output pulse width (t_w) is defined as:

$$t_w = 0.33 \times R_T C_{ext.} \ (1 + 0.7/R_T)$$

Here $R_T = 10$ K

$C_{ext} = 100$ F

therefore $t_w = 0.33 \times 10^4 \times 10^{-4} \ (1 + 0.7/10^4)$

$= 0.33$ seconds

This was found by experiment to be true.

The principle of the circuit is that the pulses from the spectrometer enter the first NAND gate IC (IC 1 on the diagram) where they are converted to positive logic pulses. They then enter the counter (IC 2 on the diagram). After two pulses are received by the system an output pulse occurs from pin 4 of the counter. This pulse is received at pin 10 of the multivibrator, (IC 3), causing the multivibrator to switch into the timing mode, i.e. the logic of pin 5 changes from low to high. This change of state has two influences. Firstly the change of state is received at a NAND gate (pin 5 of IC) which stops any subsequent pulses entering the pulse programmer, and secondly, the change of state is observed at another NAND gate (pin 2 of IC 2) which allows pulses occuring from the spectrometer to bypass the counter and continually retrigger the multivibrator. When the r.f. pulses have been stopped for

0.33 seconds the multivibrator finishes its timing, changes state, and resets the whole circuit ready for the next experiment.

An addition to this circuitry was the installation of a reset capability. This is of practical use since when setting and checking the instrumental settings of the spectrometer it is sometimes useful to use and observe a single pulse. Application of such a single pulse will be registered and countered by the circuitry. If the system is not reset the first experiment applied will cause the circuitry to count only once more giving, therefore, just one field gradient pulse (the first experiment will give no signal but subsequent experiments will be normally executed). Such a mistake would be most inconvenient since a reduced signal would be recorded. To reset the circuitry a switch was added so that a pulse could be applied to the reset pin of the multivibrator (pin 10).

An example of a CPMG pulse sequence with and without field gradient pulses is given in Figure 1.

A series of diffusion experiments on pure water were made using the modified Hahn spin-echo pulse sequence with the usual application of the field gradient pulses and the CPMG PFG sequence. The time between field gradient pulses (Δ) was varied between 10 and 600ms and plots of $\sqrt{\Delta D}$ versus Δ were made and compared to the theoretical curve (Tables 1 and 2, Figure 2). From Figure 2 it can be seen that as Δ gets large ($>$ 60ms) error is introduced, with the modified Hahn spin-echo diffusion experiment suffering the greatest loss of accuracy. A comparison of the dominant error terms of each diffusion technique is helpful.

When $G \gg G_o$ the dominant error term in the modified Hahn spin-echo is (See equation [44]).

$$- 2/3 \gamma^2 D G_o^2 \tau^3 \qquad [48]$$

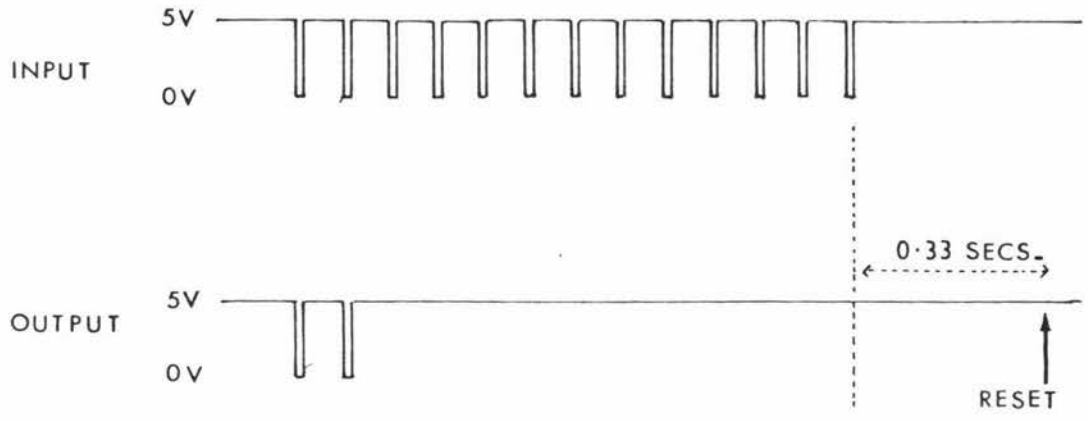
INPUT
5V
0V
0·33 SECS.
OUTPUT
5V
0V
RESET

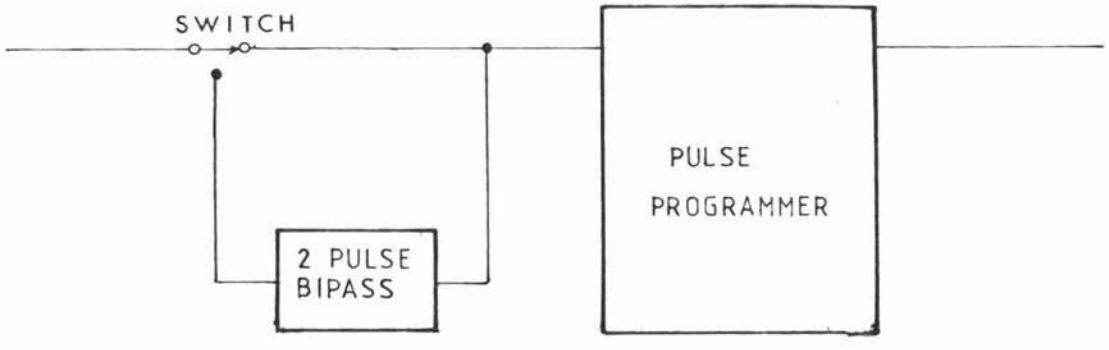
SWITCH
2 PULSE
BIPASS
PULSE
PROGRAMMER

diagram 19

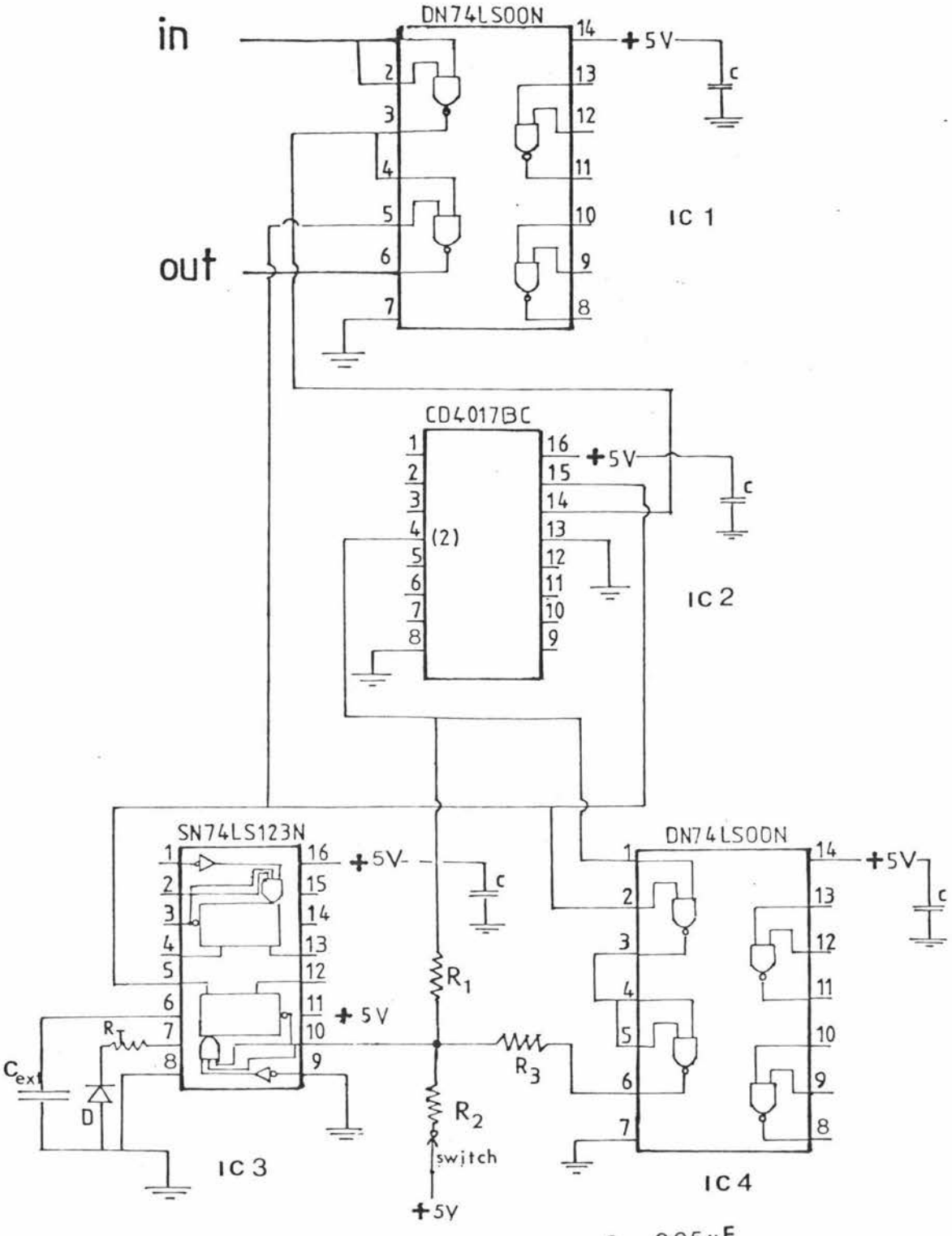

C 0·05 µF
C_{ext} 100 µF
R_1 47 KΩ
R_2 10 KΩ
R_3 670Ω
R_T 10 KΩ

diagram 20

and in the CPMG method it is (See equation [46])

$$-\left(1/12n^2\right)\gamma^2 D G_o^2 t_n^3 \qquad [49]$$

In the CMPG method n is the number of π pulses in an experiment. This equals $t_n/2\tau$. The dominant error in the CPMG method may therefore be rewritten:

$$-1/3\,\gamma^2 D \tau^2 G_o^2 t_n \qquad [50]$$

As a ratio of CPMG method/Hahn method errors:

$$\frac{\tau^2_{CPMG}\, t_n}{2\tau^3_{Hahn}} \qquad [51]$$

As an example of the errors consider an experiment with a diffusion time of 100 ms:

$$\tau_{CPMG} = 10 \text{ ms}$$

$$\tau_{Hahn} = 100 \text{ ms}$$

$$t_n = 100 \text{ ms}$$

Therefore $$\frac{\tau^2_{CPMG}\, t_n}{2\tau^3_{Hahn}} = 1/200$$

Thus when it becomes necessary to measure diffusion rates over long time intervals the use of a CPMG sequence is advantageous in reducing the systematic error.

Hahn spin-echo diffusion experiment

Δ/ms	$D/10^{-9}$ m^2 s^{-1}	$\sqrt{\Delta D}$ $/10^{-6}$m
20	2.20 (2)	6.63 (3)
50	2.26 (2)	10.6 (1)
100	2.09 (5)	14.5 (2)
150	1.99 (4)	17.3 (2)
200	1.89 (2)	19.4 (1)
300	1.73 (9)	22.8 (6)
400	1.52 (3)	24.7 (2)
500	1.27 (5)	26.0 (2)
600	1.15 (6)	26.3 (7)

Table 1

CPMG diffusion experiment

Δ/ms	$D/10^{-9}$ m^2 s^{-1}	$\sqrt{\Delta D}$ $/10^{-6}m^2$
10	2.38 (2)	4.88 (2)
50	2.26 (3)	10.6 (1)
90	2.18 (6)	14.0 (3)
130	2.26 (2)	17.1 (1)
170	2.23 (4)	19.5 (2)
210	2.23 (4)	21.6 (2)
290	2.22 (3)	25.4 (2)
370	2.18 (4)	28.4 (3)
450	2.05 (5)	30.4 (3)
570	2.13 (6)	33.8 (3)
690	2.13 (5)	38.6 (5)

Table 2

The numbers in brackets are the statistical error involved from the calculation of D. All measurements were made at 25°C.

Diffusion Distance Versus Time

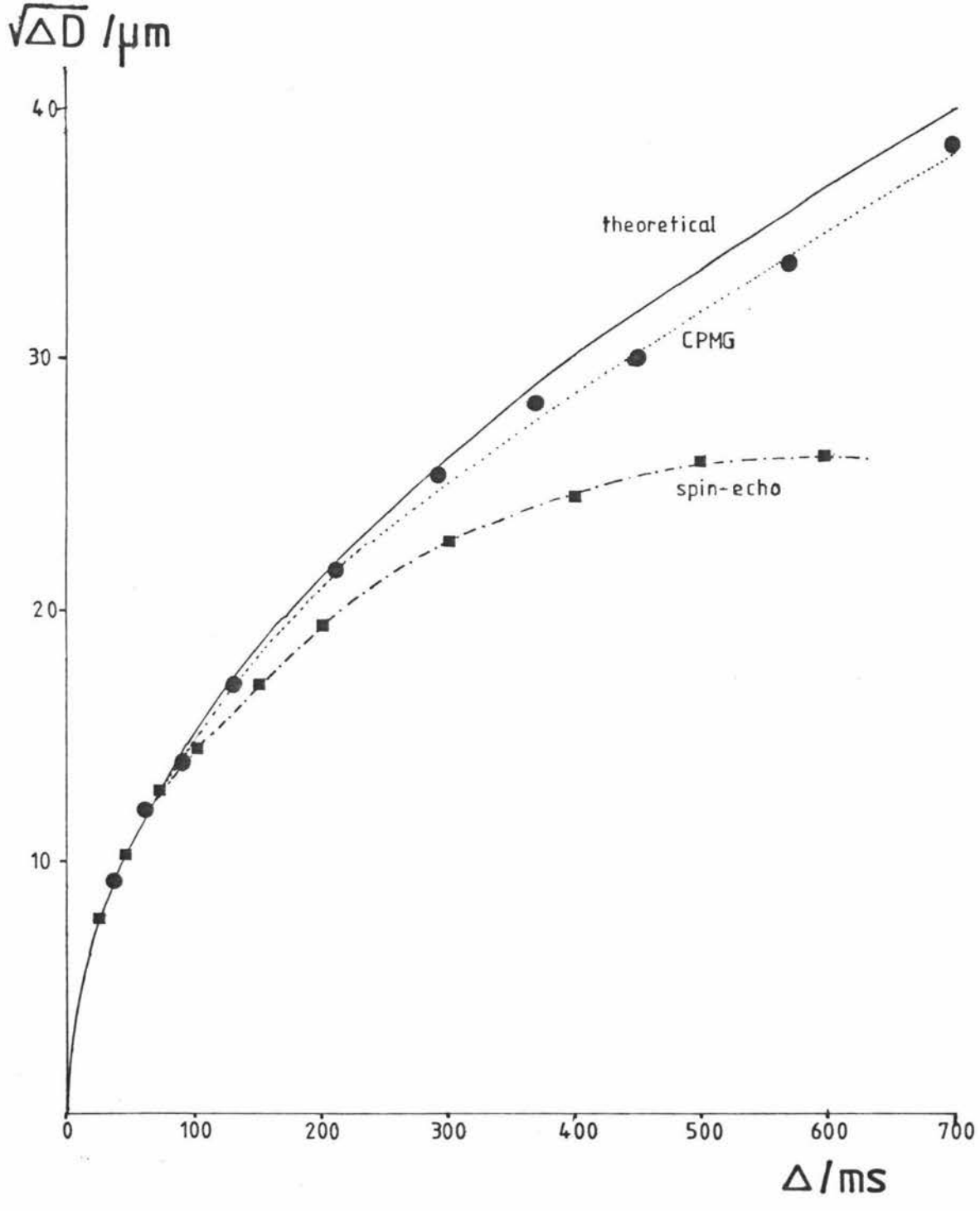

Figure 2

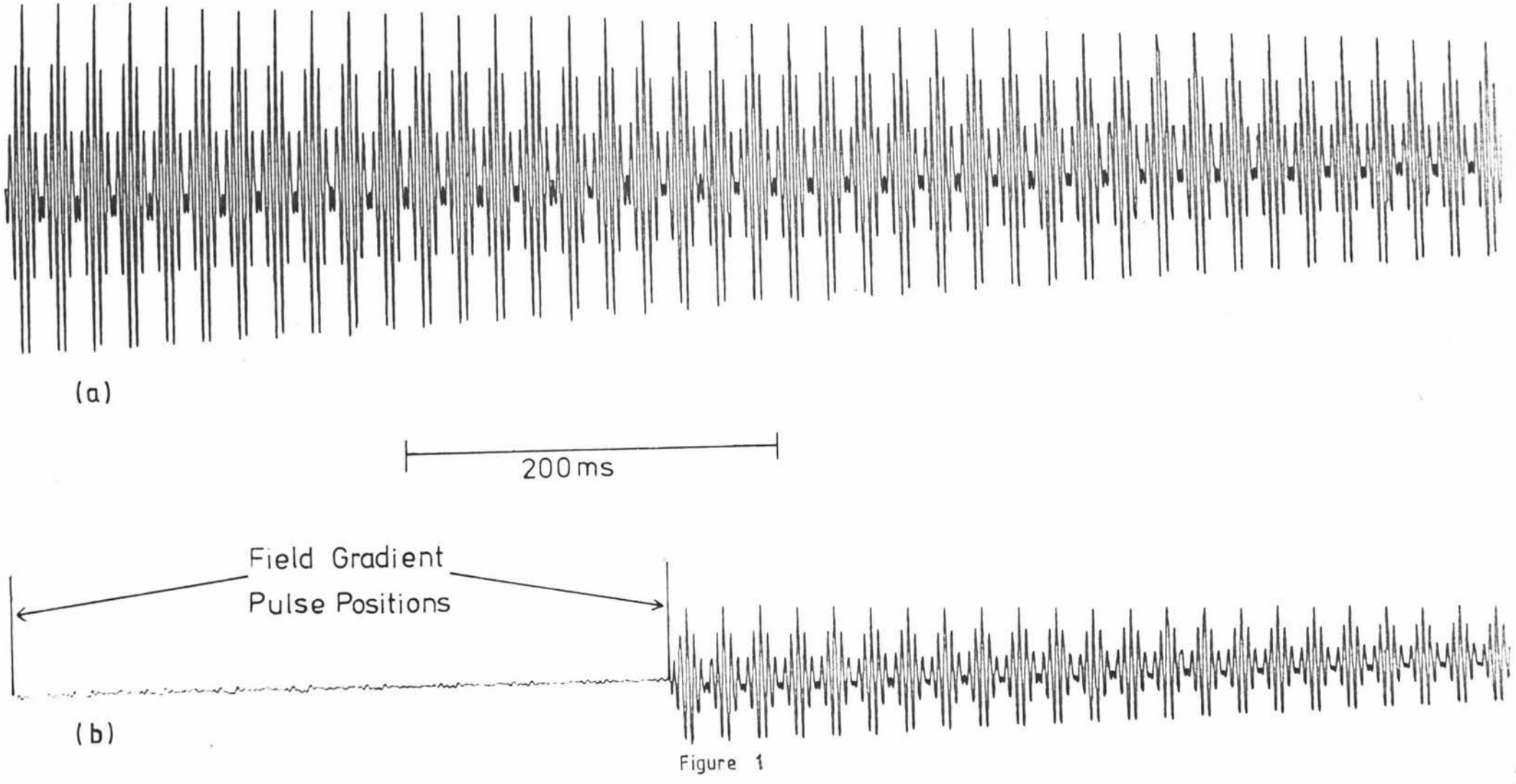

Figure 1

SECTION THREE

The Self-Diffusion of Water within the Water/CsPFO System

3.1 Introduction

The understanding of the passive transport of solute and solvent across cell membranes has practical importance for example in anaesthetics which are though to effect the permeability of membranes (14). Considerable study and speculation on possible diffusion mechanisms has therefore taken place (15). It seems certain that cell membranes consist of one or more bilayers and although consisting mainly of phospholipids the structure is basically very similar to that of surfactants in the lamellar phase (16). Diffusion studies of transport across the surfactant lamellar phase may lead to some understanding of passive diffusion across cell membranes.

3.2 Experimental

Materials; production, purification and identification.
Caesium perfluoro-octanoate (CsPFO) was prepared by neutralization of perfluoro-octanoic acid (Koch Light Laboratories Limited — England) with caesium carbonate. The caesium carbonate was prepared by the addition of a slight excess of CsCl to Ag_2CO_3 and the Cs_2CO_3 so formed separated by filtering off the AgCl precipitate and washing several times through a sintered glass filter. Drying of the Cs_2CO_3 was by rotary evaporation to near dryness and by vacuum to complete dryness. After neutralization of the perfluoro-octanoic acid the resulting CsPFO was washed thoroughly with distilled/deionized water to remove any CsCl and any excess Cs_2CO_3. The CsPFO was purified by recrystallization using a 1:1 butanol/hexane mixture and drying under vacuum for about five hours.
An initial series of tests on the purity of the CsPFO prepared was made by running infra red spectra on the original perfluoro-octanoic acid and on the final product. The final IR spectrum showed the normal red shift of the peak at $1780cm^{-1}$ which

is indicative of a carboxylic acid to carboxylate ion change, Figures 3 and 4.

3.3 Characterization of the D_2O/CsPFO System

Characterization was achieved by running a series of deuterium NMR spectra and comparing the results to those published by Boden et al. (16). The phase diagram of the D_2O/CsPFO system has been included for reference, Figure 5.

Between the weight percentages of 38% and 77% D_2O three thermotropic phases exist. Within the isotropic phase, which occurs at the highest temperatures, the perfluoro-octanoate and water molecules have entirely random orientations. Existing at lower temperatures to the isotropic phase is the nematic phase; it is thought to consist of disc shaped micelles within the aqueous continuous phase. The third liquid crystalline phase, which occurs at lower temperatures than the isotropic and nematic phases, is known as the lamellar phase. The lamellar phase consists of bilayers of amphiphile molecules in the form of crystallites alternating with layers of water molecules. If a sample is cooled from the isotropic to the lamellar phase within a magnetic field the bilayers align in a direction perpendicular to the magnetic field (diagram 21).

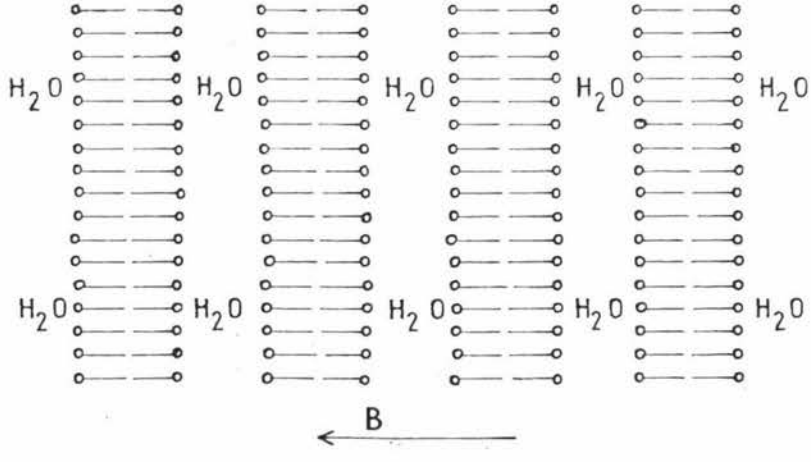

diagram 21

The various phases may be identified by deuterium NMR as follows (17, 18):

Perfluorooctanoic Acid IR Spectrum

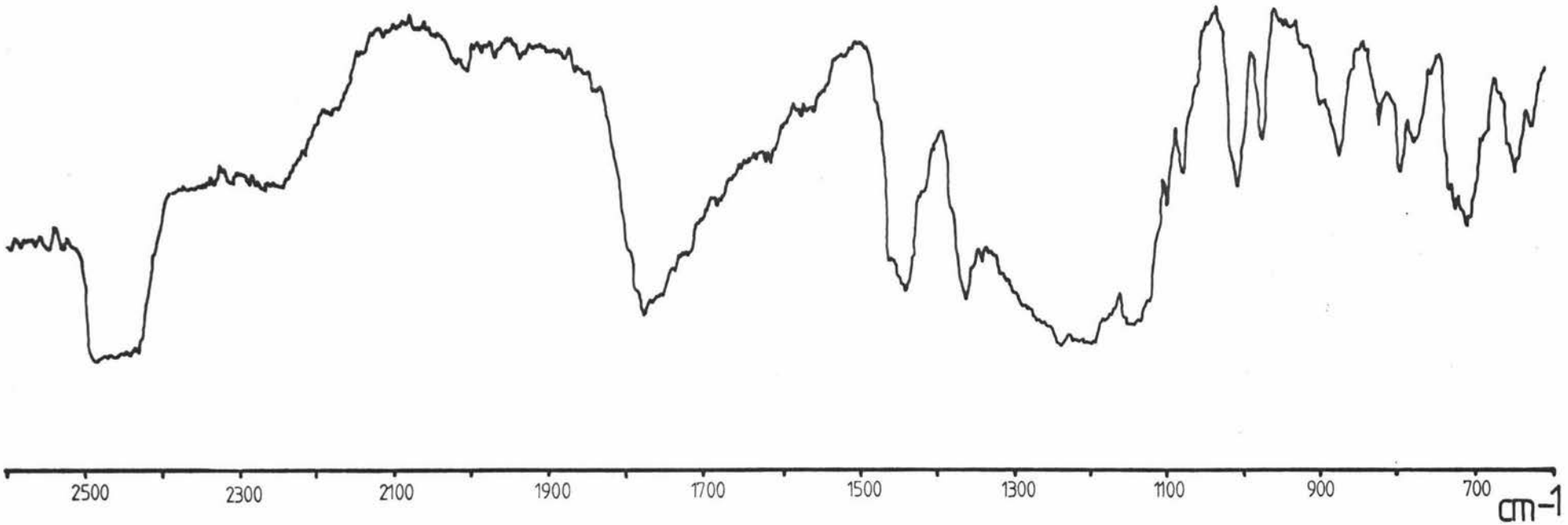

Figure 3

Caesium Perfluorooctanoate IR Spectrum
(dashed peak shows the carboxylic acid)

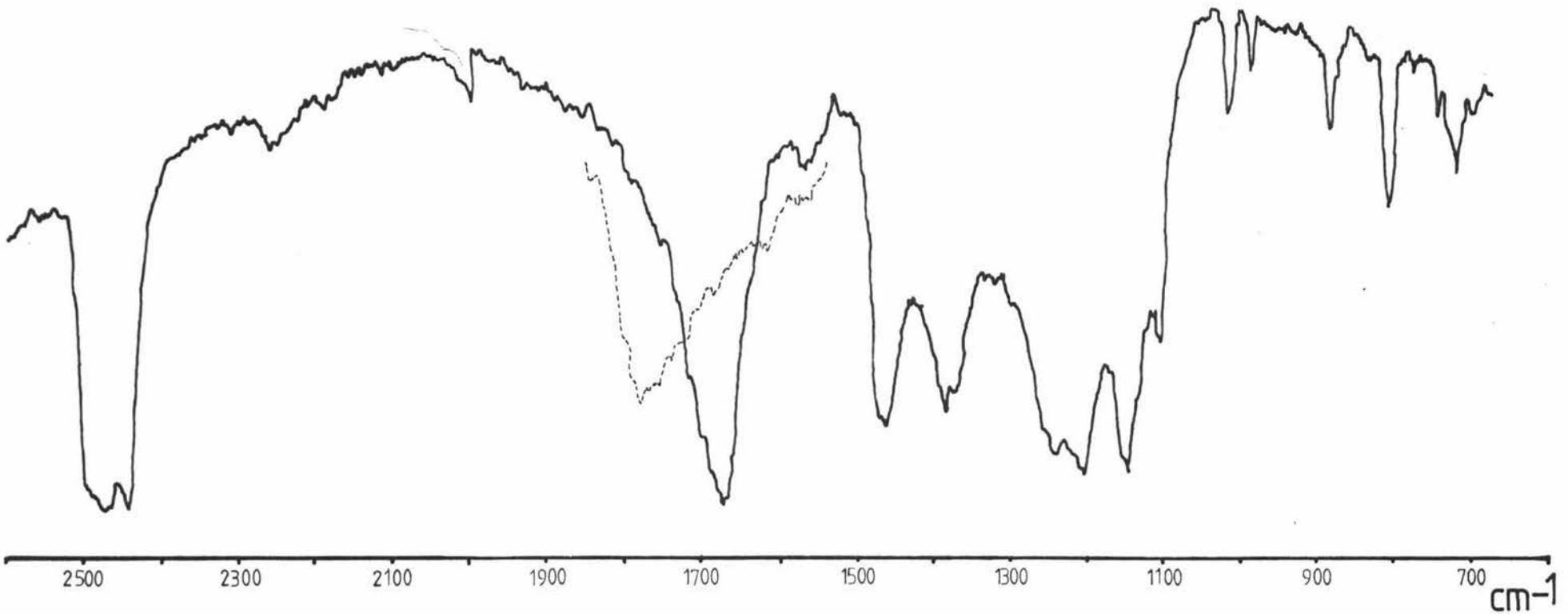

Figure 4

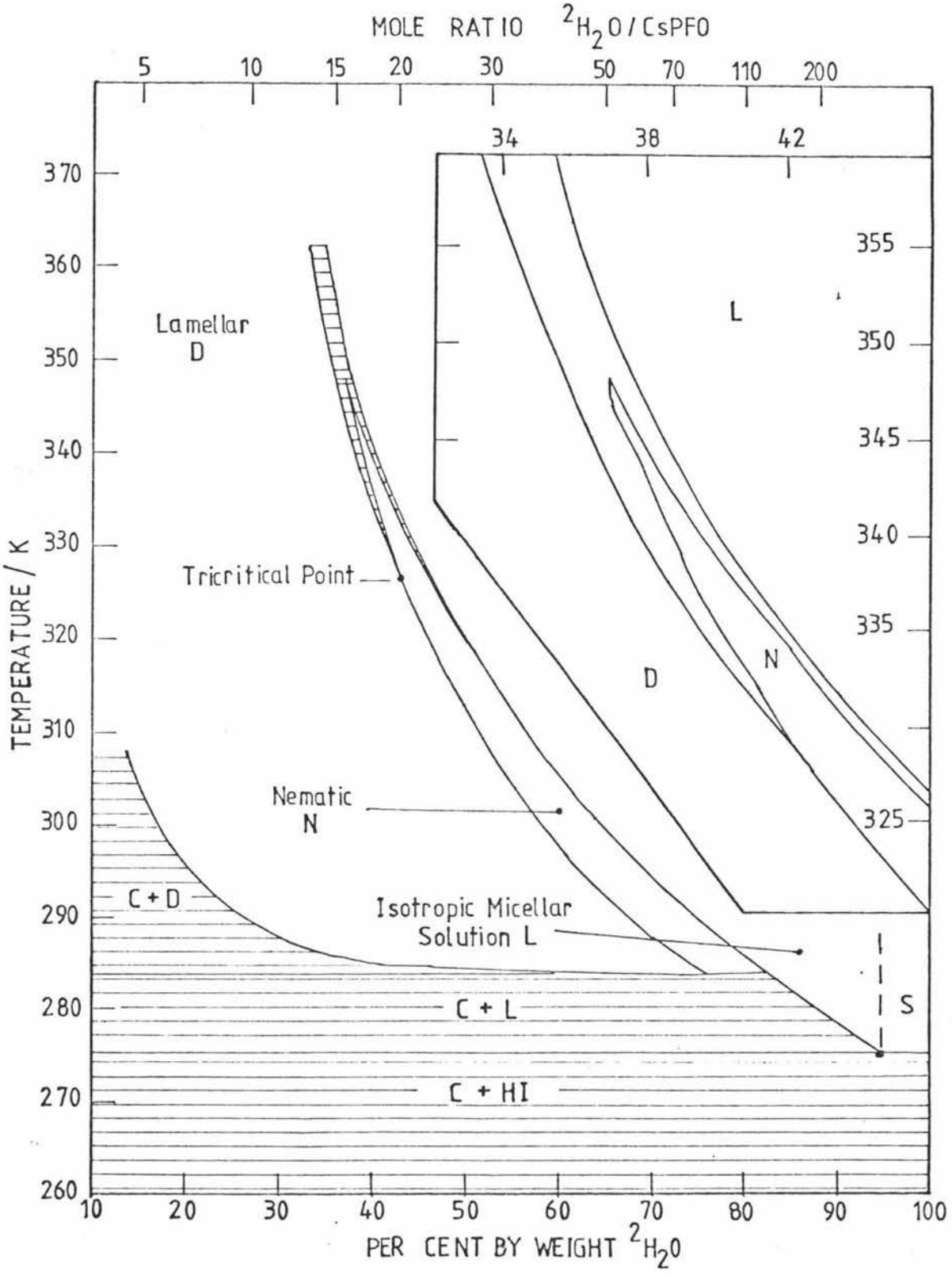
MOLE RATIO ^2H_2O / CsPFO
5
10
15
20
30
50
70
110
200
34
38
42
355
350
345
340
335
325
L
N
D
Lamellar
D
Tricritical Point
Nematic
N
C + D
Isotropic Micellar
Solution L
C + L
C + HI
S
TEMPERATURE / K
370
360
350
340
330
320
310
300
290
280
270
260
10
20
30
40
50
60
70
80
90
100
PER CENT BY WEIGHT ^2H_2O

Figure 5

(i) in the isotropic phase a single ^2H peak occurs.

(ii) in the nematic phase a doublet occurs which will reorientate upon twisting within the magnetic field.

(iii) in the ordered lamellar phase a doublet occurs which will not reorientate upon twisting within the magnetic field.

The deuterium doublet observed in the nematic and lamellar phases is a consequence of the electric quadrupolar directors being uniformly aligned. Because of the attraction of water molecules to the bilayer the reorientational motion of water becomes anisotropic on average and hence the quadrupole interaction of a deuterium spin is only partially averaged and will have cylindrical symmetry about the bilayer normal. One would expect a large doublet splitting if water molecules were permanently associated with the bilayer surface. This, however, is not observed since a fast exchange process occurs with the bulk solvent and a time averaged splitting is observed which depends both on temperature and concentration of CsPFO.

The splitting of the doublet varies according to $3\cos^2\theta-1$, where θ is the angle between the layer normal and the direction of the applied field (18). Figures 6 and 7 show the results of varying the angle θ for a 50% by weight D_2O sample at 312 K. As can be seen the $3\cos^2\theta-1$ dependence is faithfully obeyed. In this figure the splitting for, $\theta = 0^o$ is assigned the value 2.0.
To obtain the liquid crystal within the lamellar or nematic phases the samples were heated to a temperature well within the isotropic phase and then, while in the magnetic field of the spectrometer, cooled slowly at a rate of no more than two or three degrees per minute to the desired temperature. Figure 8 shows the deuterium spectra obtained upon cooling a sample from isotropic to lamellar temperatures. When a sample was within the nematic or lamellar phases the temperature was never raised. The reason for this was that layer dislocations may occur.

The phase diagram for the D_2O/CsPFO system (Boden) was reproduced and the system characterized by deuterium NMR as described above. However this technique can not be used for protons since the ^1H nucleus does not possess a quadrupole moment, but by calculating the mole ratio of ^1H_2O/CsPFO, and knowing

ANGULAR DEPENDENCE OF THE QUADRUPOLE INTERACTION

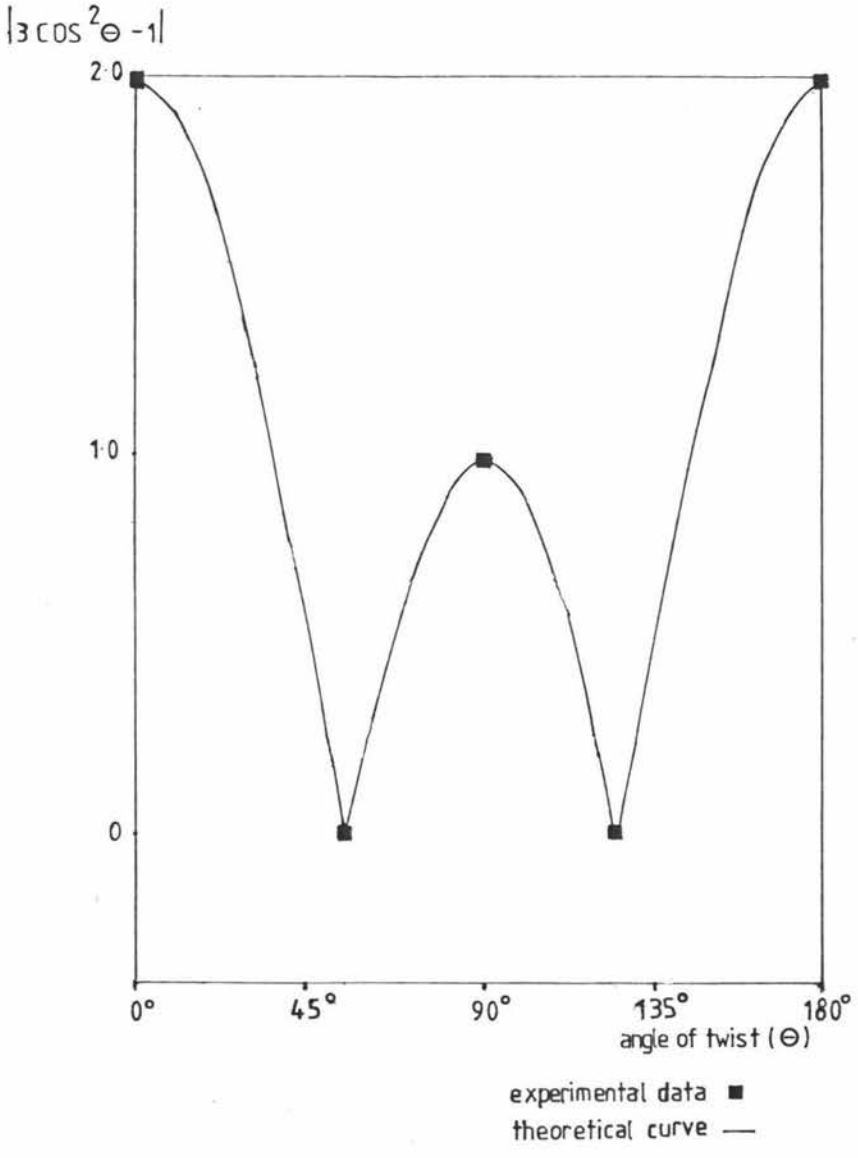

Figure 6

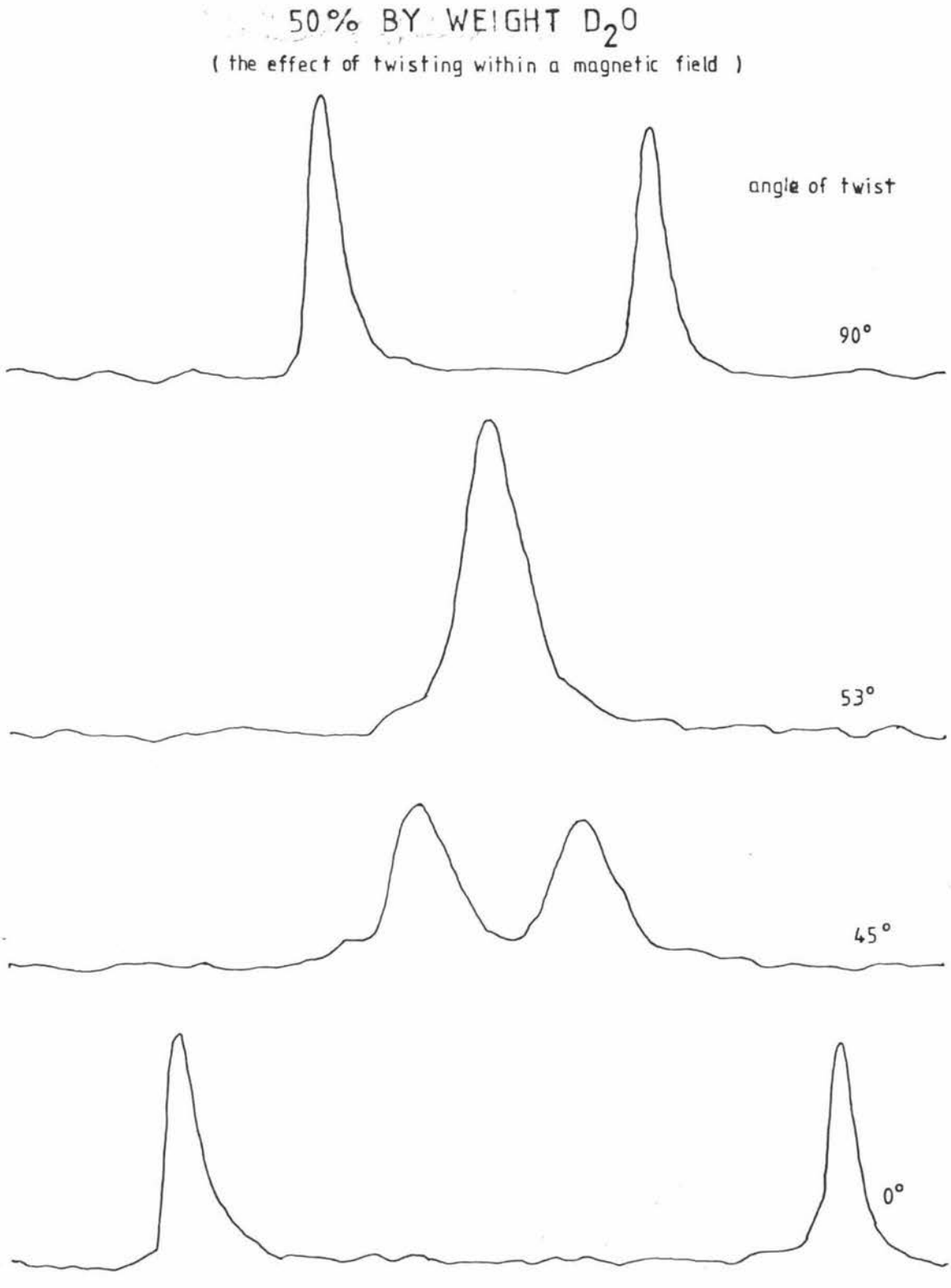
50% BY WEIGHT D_2O
(the effect of twisting within a magnetic field)
angle of twist
90°
53°
45°
0°

Figure 7

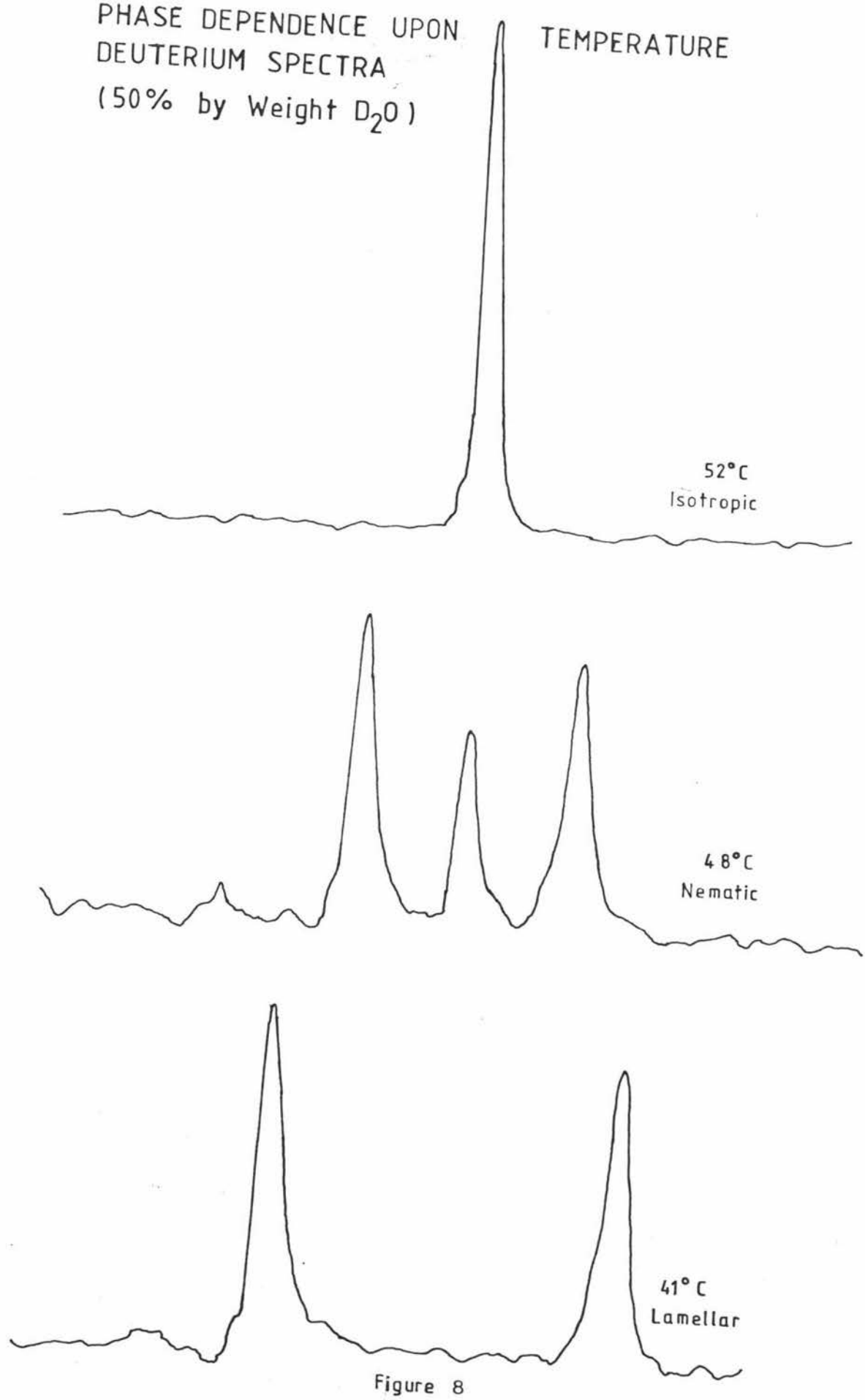
PHASE DEPENDENCE UPON TEMPERATURE
DEUTERIUM SPECTRA
(50% by Weight D_2O)
52°C
Isotropic
48°C
Nematic
41°C
Lamellar

Figure 8

the temperature for any given sample, the liquid crystalline structure may be deduced from the phase diagram.

All the ^{2}H spectra were made on relatively large samples in 10 mm O.D. tubes. Because the $^{1}H_2O$/CsPFO proton studies were made on samples in 4 mm O.D. tubes there was the possibility of surface orientational effects becoming important. A deuterium spectra was, therefore, run on a 64% by weight D_2O sample in a 4 mm O.D. tube placed within a 10 mm O.D. tube (diagram 22). The spectra showed all the isotropic, nematic and lamellar properties at the expected temperatures (Figure 9).

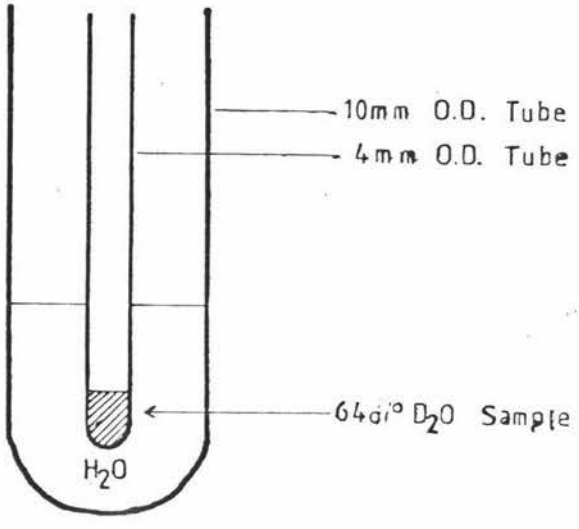

diagram 22

3.4 Results and discussion

Measurements of the self-diffusion of $^{1}H_2O$ by PFG NMR were made on the $^{1}H_2O$/CsPFO system at various temperatures and weight percentages. For each weight percentage self-diffusion coefficients were determined over a temperature range wide enough to include the isotropic, nematic and lamellar phases, and in all measurements a least squares analysis was performed and statistical errors calculated. Results are shown tabulated in Tables 3 to 8 and as Arrhenius plots in Figures 10 to 15. For all self-diffusion coefficient measurements Δ = 10 ms, δ = 2 ms and 2τ = 16 ms.

64% BY WEIGHT D_2O SAMPLE WITHIN A 4mm O.D. TUBE

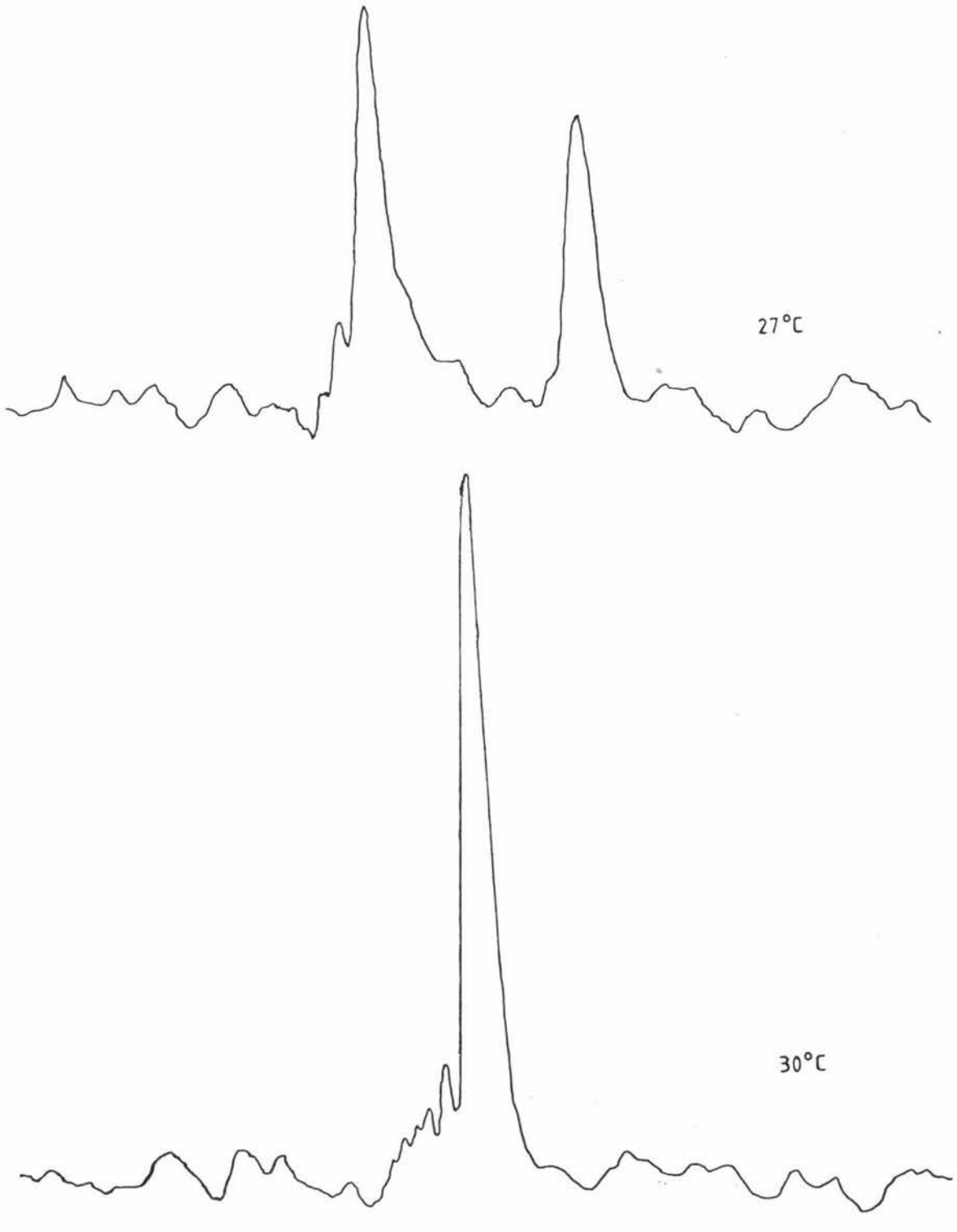

Figure 9

The discussion which follows will concentrate almost entirely on the 46% and 52% by weight water samples since these were the only samples which showed the expected $D_{||}/D_{\perp}$ anisotropy due to the difficulty of producing consistent sample orientations on cooling from the isotropic to the lamellar region. Slow cooling was necessary and a useful pair of results took several hours to obtain. This difficulty in obtaining sample reproducibility has previously been experienced by Boden et al. (17).

Despite all the care taken the Arrhenius plots have scatter well outside the statistical errors involved in the calculation of the diffusion coefficients. One possible explanation is the presence of impurities within the sample. The two possible types of impurity are paramagnetic and nonparamagnetic. The presence of paramagnetic impurities adhering to the inside of the tube could cause anisotropy of diffusion since such material interferes with the pulsed field gradient magnetic flux. This effect would be the same in all phases and so a measure of the error may be obtained from the isotropic phase, where no anisotropy should exist. Refering to Table 4 and Figure 14, for example, one observes that within experimental error $D_{\perp}$ equals $D_{||}$ in the isotropic region.

38% by Weight Water

Temp./^{o}C	(Temp./K)$^{-1}10^{-3}$	$(D_{\perp}\ D_{||})/10^{-9} m^2 s^{-1}$	$D_{||}/D_{\perp}$
44.0	3.153	1.83 (1)	
62.8	2.976	2.22 (1) 2.14 (2)	
67.5	2.935	2.70 (2)	
67.8	2.933	2.97 (2) 2.89 (2)	
70.0	2.914	3.25 (3)	
75.5	2.868	3.40 (3)	
81.0	2.823	4.2 (2)	

Activation Energy (1) 19 kJ/mole

The numbers in brackets are the errors involved in the last figure.

Table 3

46% by Weight Water

Temp./°C	$(Temp./K)^{-1}.10^{-3}$	$(D_{\perp}$ $D_{\parallel})/10^{9}m^{2}s^{-1}$		$D_{\parallel}/D_{\perp}$
22.0	3.388	0.850(7)	1.657(9)	1.95 (3)
24.4	3.360	0.964(6)	1.74 (1)	1.80 (2)
24.6	3.358	0.950(7)	1.76 (1)	1.85 (2)
27.0	3.331	1.008(5)	1.84 (1)	1.83 (2)
30.2	3.296	1.129(7)	1.972(9)	1.75 (2)
32.5	3.271	1.243(7)	2.05 (1)	1.65 (2)
35.0	3.245	1.317(5)	2.08 (2)	1.58 (1)
36.8	3.226	1.419(9)	2.16 (2)	1.52 (2)
38.0	3.213	1.63 (1)	2.00 (2)	1.23 (2)
38.9	3.204	1.54 (1)	2.17 (2)	1.40 (2)
40.7	3.186	1.40 (2)	2.14 (3)	1.53 (4)
42.5	3.168	1.820(8)	1.84 (1)	1.01 (1)
44.7	3.146	1.65 (2)	1.85 (1)	1.12 (2)
45.0	3.143	2.19 (1)	2.09 (1)	0.954(9)
45.5	3.138	2.00 (4)	1.90 (4)	0.95 (4)
47.0	3.123	2.33 (2)	1.97 (2)	0.85 (2)
47.8	3.115	2.30 (3)		
49.2	3.102	2.35 (4)	2.35 (3)	1.00 (3)
50.9	3.085	2.420(5)	2.45 (1)	1.012(6)

Activation Energy ($\perp$) 23 kJ/mole

Table 4

47% by Weight Water

Temp./^{o}C	(Temp./K)$^{-1}$.10^{3}	($D_{\perp}$ $D_{\parallel}$)/10^{-9}m^{2}s^{-1}	$D_{\parallel}/D_{\perp}$
29.7	3.301	1.594(6) 2.17 (6)	1.36 (4)
42.5	3.168	1.716(7) 1.813(5)	1.057(7)
54.6	3.051	2.71 (2) 2.689(9)	0.99 (1)
61.7	2.986	3.00 (1) 2.97 (2)	0.99 (1)
70.5	2.910	3.41 (2) 3.55 (1)	1.041(9)
82.0	2.815	4.11 (2) 4.28 (4)	1.04 (1)

Activation Energy ($\perp$) 17 kJ/mole

Table 5

This shows that paramagnetic impurities are not a dominant error. The remaining type of impurity to consider is the presence of non-paramagnetic material. Non-paramagnetic impurities would not necessarily show in the isotropic phase but may lead to significant dislocations in the bilayer structure. This can not be overruled as the sensitivity of the bilayer structure to impurities is unknown, but great care was taken in sample preparation so such error is unlikely.

Another possible contribution to the observed scatter is inexact twisting of the sample tube by 90^{o} since an error in rotation of about 5^{o} is possible. Because orientation of the bilayers is due to the magnetic field of the spectrometer $D_{\perp}$ measurements will have perfect alignment across the lamellar phase and will have no angular error unless the sample is rerotated to perhaps repeat measurements. To obtain $D_{\parallel}$ measurements a rotation of the sample tube is made and an error is introduced. However $\pm$ 5^{o} is small and should have little effect on such measurements. It is observed that $D_{\parallel}$ results have the greatest scatter, but this difference is slight.

52% by Weight Water

Temp./^{o}C	(Temp./K)$^{-1}$.10^{3}	($D_{\perp}$ $D_{\parallel}$)/10^{-9}m^{2}s^{-1}	$D_{\parallel}/D_{\perp}$
22.0	3.388	1.09 (1) 1.074 (8)	.99 (2)
22.5	3.382	1.08 (1) 1.78 (2)	1.65 (3)
22.7	3.380	1.129(9) 1.77 (1)	1.57 (2)
23.5	3.370	1.08 (1) 1.81 (2)	1.68 (3)
24.5	3.359	1.22 (2)	
24.8	3.356	1.18 (1) 1.84 (1)	1.56 (2)
25.0	3.353	1.15 (1)	
26.7	3.334	1.27 (1) 1.904 (6)	1.50 (2)
28.0	3.320	1.24 (1) 1.90 (1)	1.53 (2)
29.1	3.308	1.23 (1) 2.00 (1)	1.63 (2)
29.2	3.307	1.27 (1) 1.91 (1)	1.50 (2)
29.6	3.302	1.322(6) 1.98 (2)	1.50 (2)
29.7	3.301	1.36 (1) 2.033 (7)	1.49 (2)
29.7	3.301	1.33 (1) 1.97 (2)	1.48 (3)
30.0	3.298	1.30 (1) 2.06 (1)	1.58 (2)
30.3	3.295	1.23 (2) 1.97 (1)	1.60 (3)
31.0	3.287	1.44 (2) 1.73 (2)	1.20 (3)
31.6	3.281	1.334(7)	
32.0	3.277	1.57 (1) 1.58 (1)	1.01 (1)
33.0	3.266	1.560(8) 1.62 (3)	1.04 (2)
33.2	3.264	1.48 (2) 2.16 (1)	1.46 (3)
33.5	3.261	1.64 (2) 1.59 (1)	.97 (2)
33.8	3.257	1.47 (1) 1.64 (2)	1.12 (2)
35.9	3.235	1.78 (2) 1.75 (1)	.98 (1)
36.0	3.234	1.86 (1) 2.27 (4)	1.22 (3)
36.8	3.226	1.67 (3) 1.70 (1)	1.02 (2)
39.0	3.203	1.999(7) 1.98 (1)	.990(8)
39.5	3.198	2.02 (2) 1.958 (8)	.97 (1)
55.7	3.040	2.81 (1)	

Activation Energy ($\perp$) 19.4 kJ/mole

Table 6

56% by Weight Water

Temp./°C	$(\text{Temp./K})^{-1}.10^3$	$(D_\perp$	$D_{\parallel})/10^{-9}m^2s^{-1}$	D_{11}/D_1
23.5	3.370	1.214(5)	1.75 (1)	1.44(1)
24.0	3.365	1.16 (2)	1.69 (1)	1.46(3)
24.5	3.359	1.40 (2)	1.524 (7)	1.09(2)
24.5	3.359	1.39 (1)		
31.5	3.282	1.94 (2)		
34.8	3.247	2.088(9)		
39.5	3.198	2.38 (2)		
44.0	3.153	2.55 (4)		
47.0	3.123	2.87 (2)		
54.0	3.056	3.13 (3)		

Activation Energy (⊥) 20 kJ/mole

Table 7

60% by Weight Water

Temp./°C	$(\text{Temp./K})^{-1}.10^3$	$(D_\perp$	$D_{\parallel})/10^{-9}m^2s^{-1}$	D_{11}/D_1
20.4	3.406	1.226(4)	1.286 (5)	1.016 (7)
21.6	3.392	1.381(6)	1.30 (1)	0.94 (7)
24.3	3.361	1.554(5)	1.515 (3)	0.975 (5)
27.8	3.322	1.68 (1)	1.682 (6)	1.00 (1)
29.0	3.309	1.937(7)	1.939 (8)	1.001 (8)
30.1	3.297	2.08 (1)	2.041 (6)	0.981 (8)
33.8	3.257	2.09 (1)	2.11 (2)	1.01 (1)
37.0	3.224	2.19 (1)	2.17 (1)	0.991 (9)
41.5	3.178	2.54 (2)	2.62 (8)	1.03 (4)
47.0	3.123	2.81 (2)	2.73 (1)	0.97 (1)
47.7	3.116		2.805 (6)	
57.6	3.023	3.47 (1)	3.49 (1)	1.01 (1)
68.0	2.931	3.95 (2)	3.99 (3)	1.01 (1)
71.0	2.905	4.224(9)	4.15 (2)	0.982 (7)

Activation Energy (⊥) 16 kJ/mole
26

Table 8

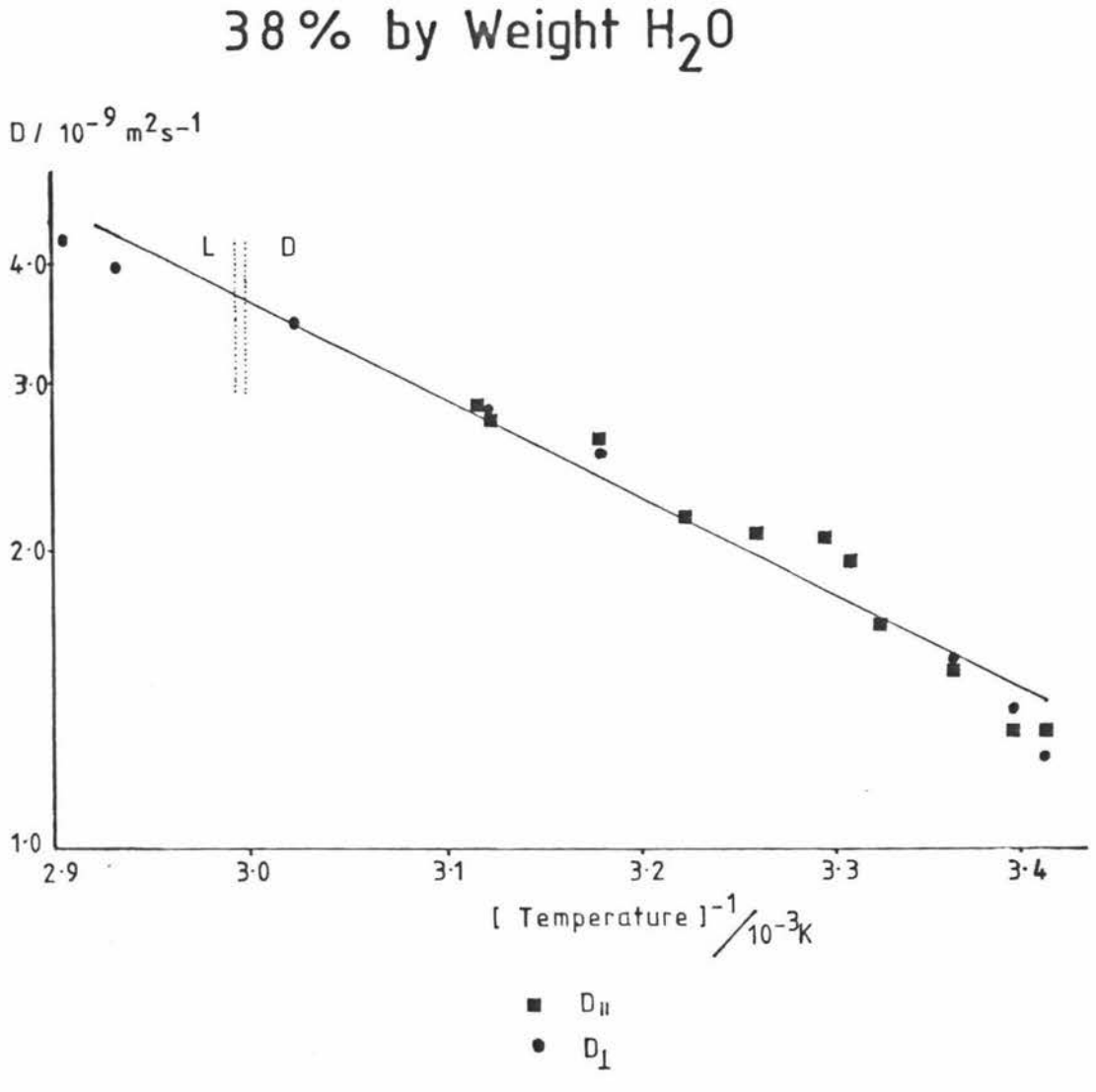
38% by Weight H_2O
D / 10^{-9} m^2s^{-1}
4·0
3·0
2·0
1·0
L
D
2·9
3·0
3·1
3·2
3·3
3·4
[Temperature]$^{-1}$ / 10^{-3}K
D_{II}
$D_{\perp}$

Figure 10

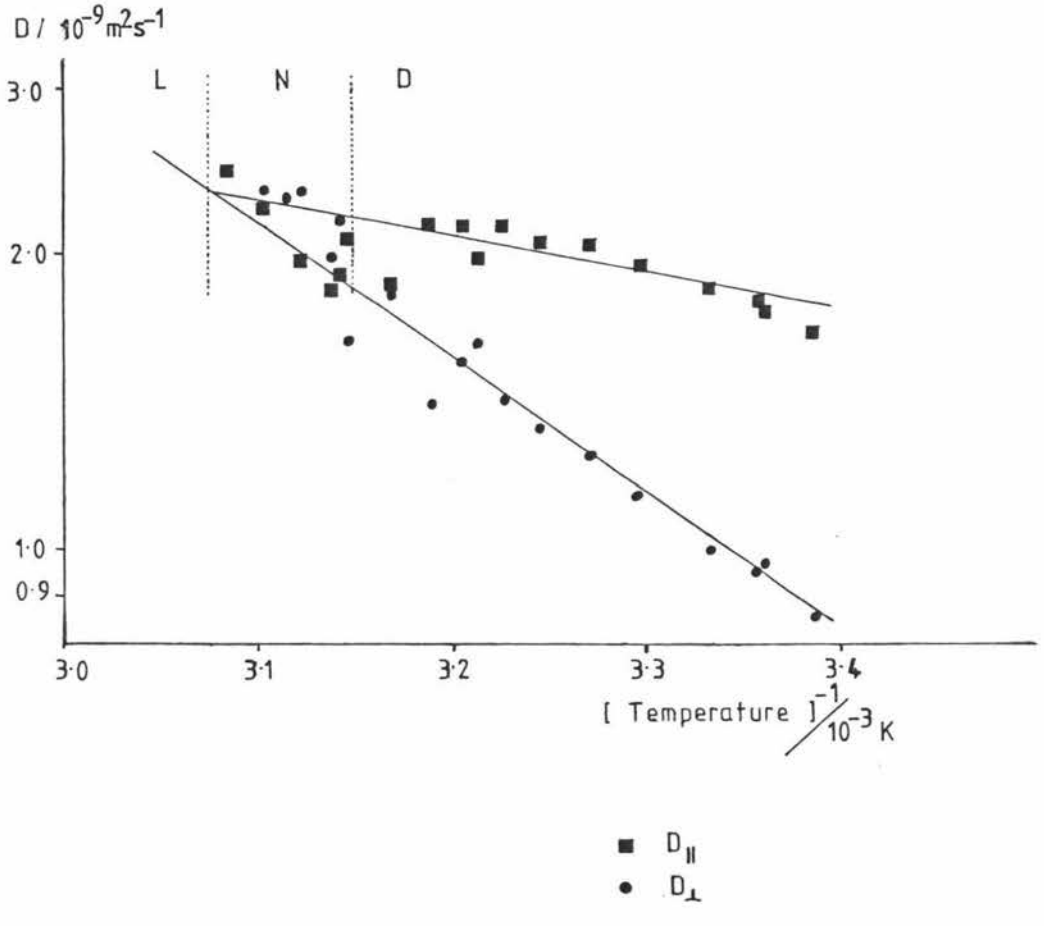
46% by Weight H_2O
D / $10^{-9}m^2s^{-1}$
L
N
D
3·0
2·0
1·0
0·9
3·0
3·1
3·2
3·3
3·4
[Temperature]$^{-1}$ / 10^{-3} K
$D_{\parallel}$
$D_{\perp}$

Figure 11

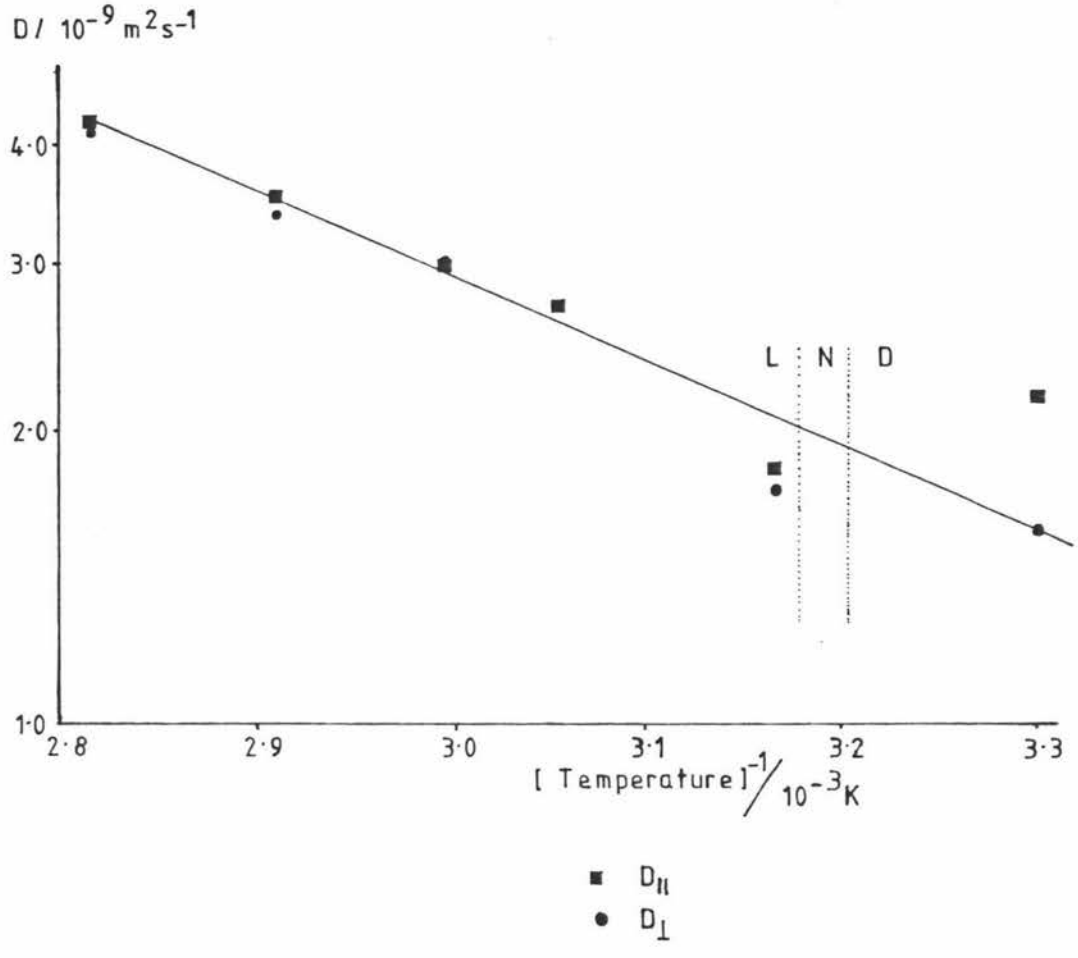
47% by Weight H_2O
D / 10^{-9} m^2s^{-1}
4·0
3·0
2·0
1·0
L
N
D
2·8
2·9
3·0
3·1
3·2
3·3
[Temperature]$^{-1}$ / 10^{-3}K
$D_{\parallel}$
$D_{\perp}$

Figure 12

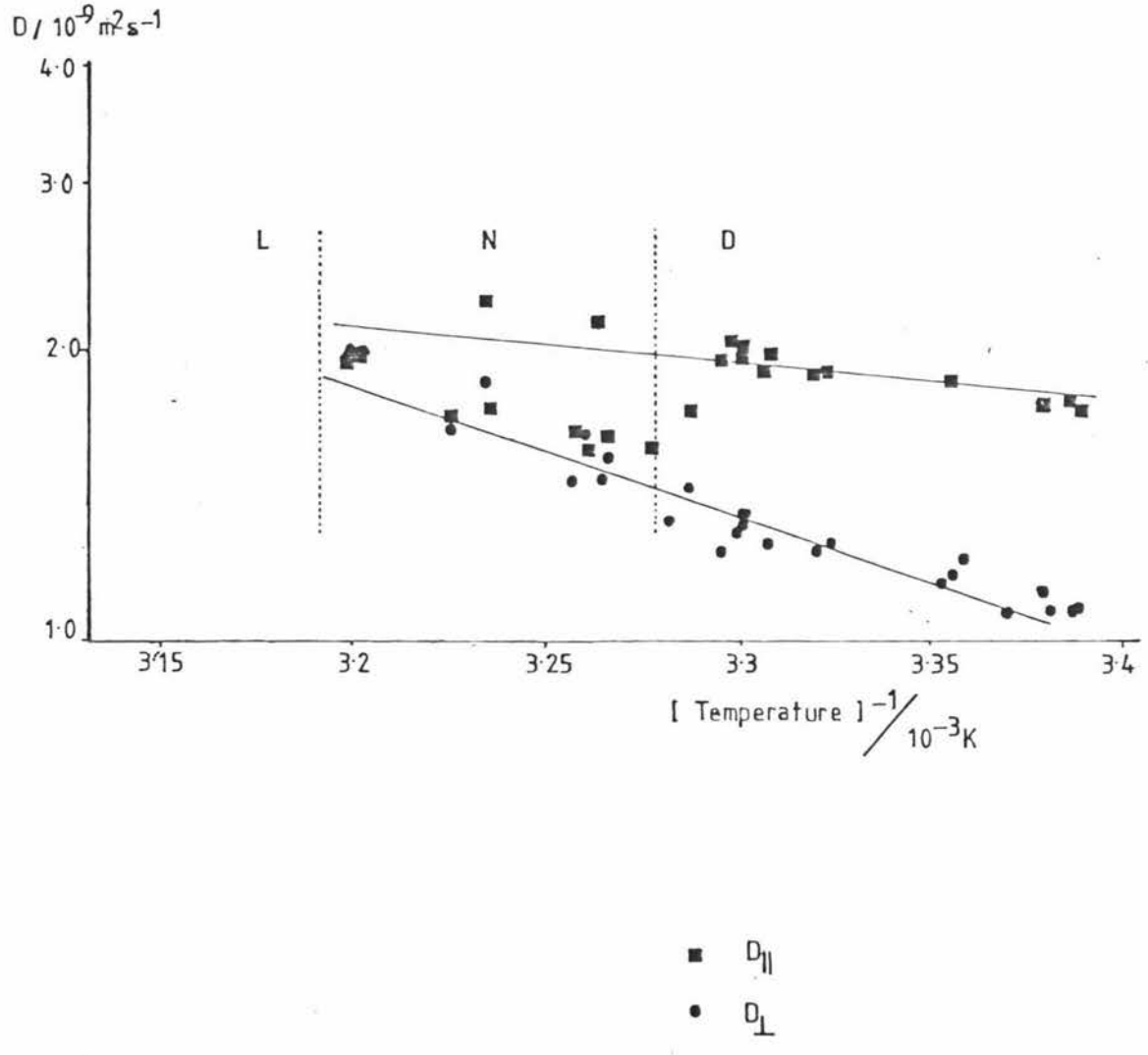
52 % by Weight H_2O
D / 10^{-9} m^{2}s^{-1}
4·0
3·0
2·0
1·0
L
N
D
3·15
3·2
3·25
3·3
3·35
3·4
[Temperature]$^{-1}$ / 10^{-3}K
$D_{\parallel}$
$D_{\perp}$

Figure 13

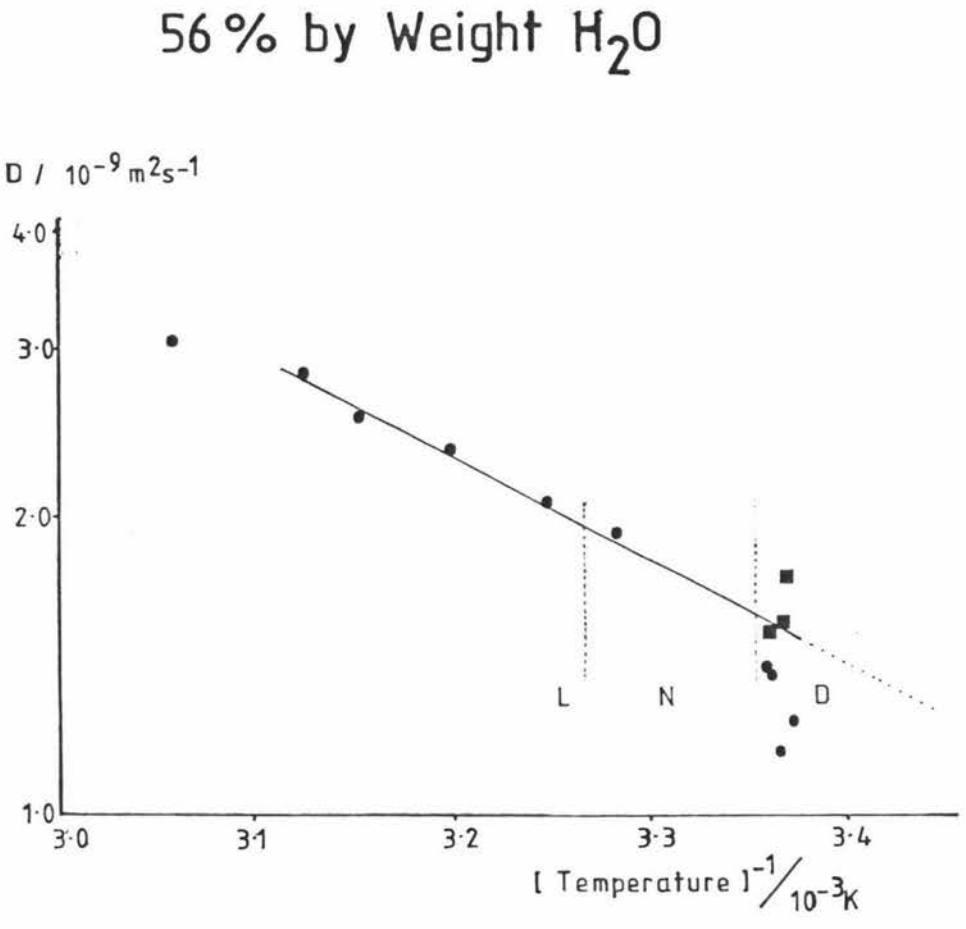
56 % by Weight H_2O
D / 10^{-9} $m^2 s^{-1}$
4·0
3·0
2·0
1·0
L
N
D
3·0
3·1
3·2
3·3
3·4
[Temperature]$^{-1}$ / 10^{-3} K

Figure 14

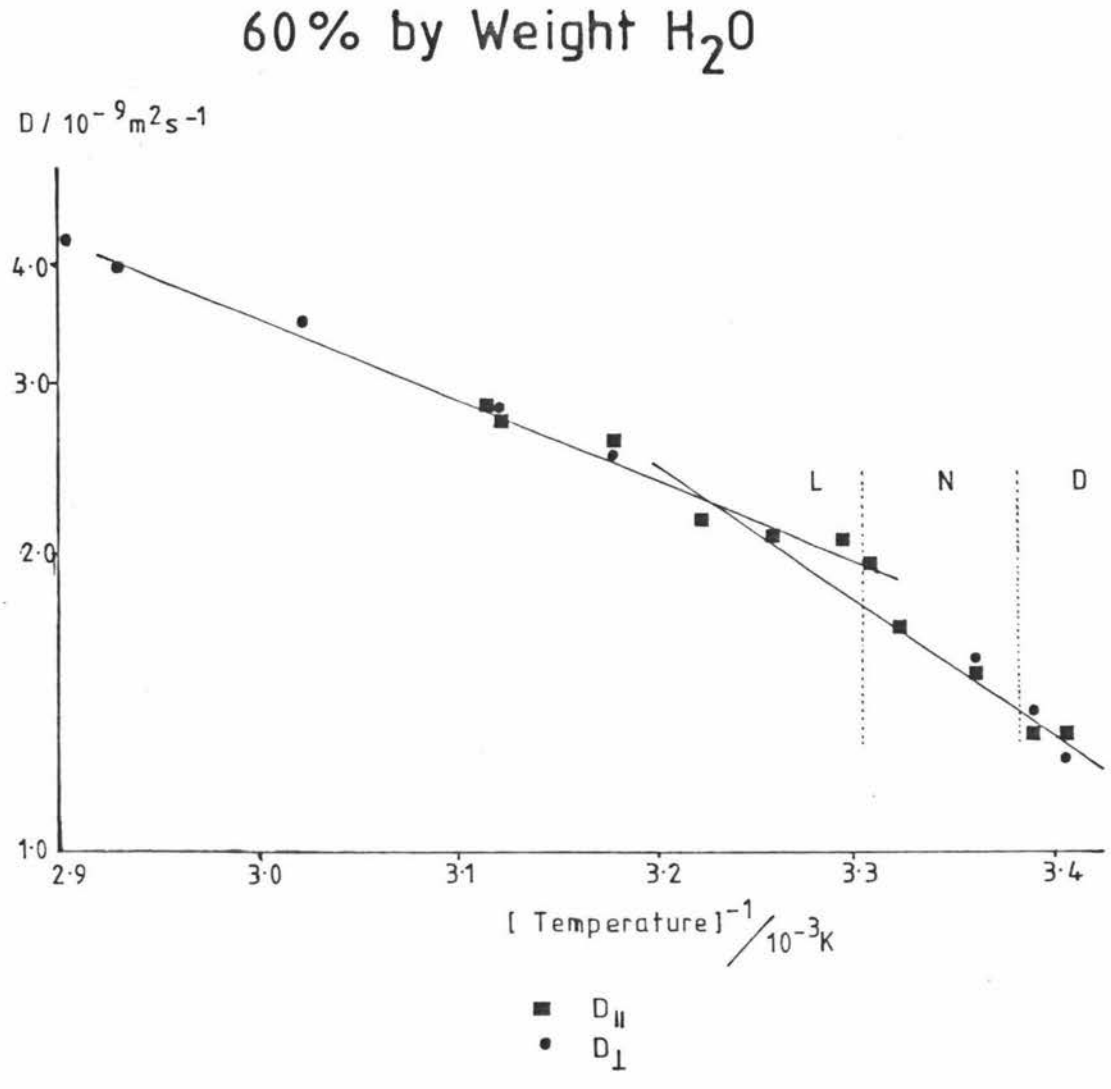
60% by Weight H_2O
D / $10^{-9} m^2 s^{-1}$
4·0
3·0
2·0
1·0
L
N
D
2·9
3·0
3·1
3·2
3·3
3·4
[Temperature]$^{-1}$ / 10^{-3}K
$D_{\parallel}$
$D_{\perp}$

Figure 15

The sources of errors discussed above are unlikely to fully account for the observed scatter. It seems likely that thermodynamic irregularities are occuring at the positions of greatest scatter. Why these exist is only speculative but temperature variation is probably critical within these regions. Any sudden lowering or increase in temperature may affect the bilayer formation and stability. A similar conclusion was reported by Boden in a personal communication.

The fact that the deuterium NMR of orientated samples shows good doublet resolution does not preclude the possibility of dislocations in the bilayers. The rate of cooling is an extra variable which could well determine the extent of dislocation and so a fixed cooling rate was adopted (2K min^{-1}) for all samples.

In all the measurements of the water diffusion rate parallel to the bilayers, $D_{||}$, and perpendicular to the bilayers, $D_{\perp}$, the plots of ln [A(G)/A(o)] versus G^2 were linear, indicating that no restricted diffusion occurs over the experimental diffusion distance.

i.e. $\bar{z}^2$ = $2D(\Delta - \delta/3)$ refer to equation [pp22] in theory

= $2 \times 2 \times 10^{-9}(10-2/3) \times 10^{-3} m^2$

= $3.7 \times 10^{-11}\ m^2$

RMS distance $\sim$ 6000nm

A similar conclusion was obtained on the lithium perfluorooctanoate system by Tiddy (19). It is also noticeable that there is only one discontinuity in the diffusion rates, occuring at the nematic/lamellar phase transition. For the most dilute solution, 60% by weight H_2O, where the N/D boundary is approximately at room temperature, no anisotropy in the diffusion rate was observed. This could well be due to the fact that the system was in the N rather than the D phase. For the more concentrated samples anisotropy is evident below the N/D boundary temperature. In each case, however, the anisotropy is small with values of $D_{||}/D_{\perp}$ being typically around 1.4 but never greater than 2.0. Previous work has shown that the distance between bilayers of surfactants such as CsPFO is a function of the water content, but still of the order of 1.5 nm (20). If the water was confined between the bilayers no attenuation of the echo amplitude on application of the field gradient would be observed since

in practice $\bar{z}^{-2}$ is required to be $> (100\ nm)^2$ for any significant attenuation in the echo to occur (11). The fact that there is a measureable diffusion rate perpendicular to the bilayers means that water is getting through. In fact it is diffusing through the layers without too much difficulty. A $D_\perp : D_{11}$ ratio of 0.7 which is typical in this study may be compared to an isotropic protein water system (20) where the pure water diffusion coefficient can be reduced to $0.7\ D_o$ at about 15% protein by weight. The reduction is simply an obstruction and hydration effect (21). While CsPFO is much smaller than protein molecules the concentrations used in this study are much greater and hydration at the polar head groups could well lead to an attenuation of the free water diffusion coefficient.

An explanation for the penetration of surfactant layers and membranes by solvent has often been explained by the presence of relatively large defects or holes. Water (or solvent) is considered to move across the membrane via pores of sufficient size so that the water inside them has essentially bulk properties. Using this model pores as small as 30 nm have been calculated in biological membranes (22). One expects at most a small energy barrier to be encountered by a water molecule entering the pore; within the pore the only energy barriers are those due to the diffusive or viscous resistance and thus the effective energy barrier for permeation is the activation energy for the self-diffusion of free water $\sim$ 19 kJ/mole.

Tiddy has studied the H_2O/LiPFO system and concluded that a large pore model is incongruous with the data (19). The results presented in this thesis also do not conform to a large pore model. Take, for example, the 52% by weight water sample at $\sim$ 300K which has a $D_\perp \sim 1.3 \times 10^{-9} m^2 s^{-1}$. Since the distance between adjacent bilayers is of the order of 1.5 nm (23) any diffusion over this distance will be undetectable with the pulse spacings used here. The diffusion rate of water between adjacent bilayers will therefore be seen to be very much slower than that of the free water which travels through the holes, diagram 23.

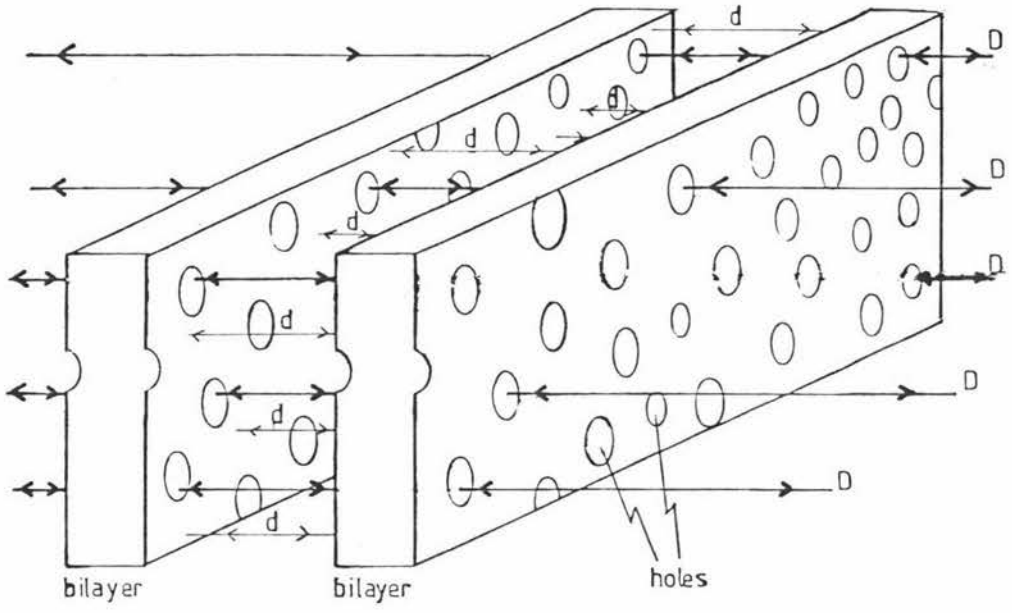

diagram 23

Therefore (refering to diagram 23)

$D_{\perp}$ = d between adjacent bilayers x Percentage of Surface in Bilayers

+ D free water x Percentage of Surface in Cracks or Holes

and since d between adjacent bilayers $\ll$ D free water

the percentage of the surface area of a bilayer in cracks or holes

$$= \frac{D_{\perp}}{D_{H_2O}} \times 100$$

$$= 50\%$$

Using the similar liquid crystal LiPFO Tiddy et al. (19) found that the lithium ion diffusion showed a larger anisotropy of diffusion than did water, with a $D_{||}/D_{\perp}$ value of approximately 1.92 compared to a water $D_{||}/D_{\perp}$ value of approximately 1.38. Therefore more than 50% of the water transport must occur in regions small enough to exclude the diameter of a hydrated lithium ion, $\sim$ 0.5nm. If the diameter of the holes, or cracks, are on average smaller than 0.5 nm diameter and 50% of the bilayer consists of such holes or cracks then (refering to diagram 24):

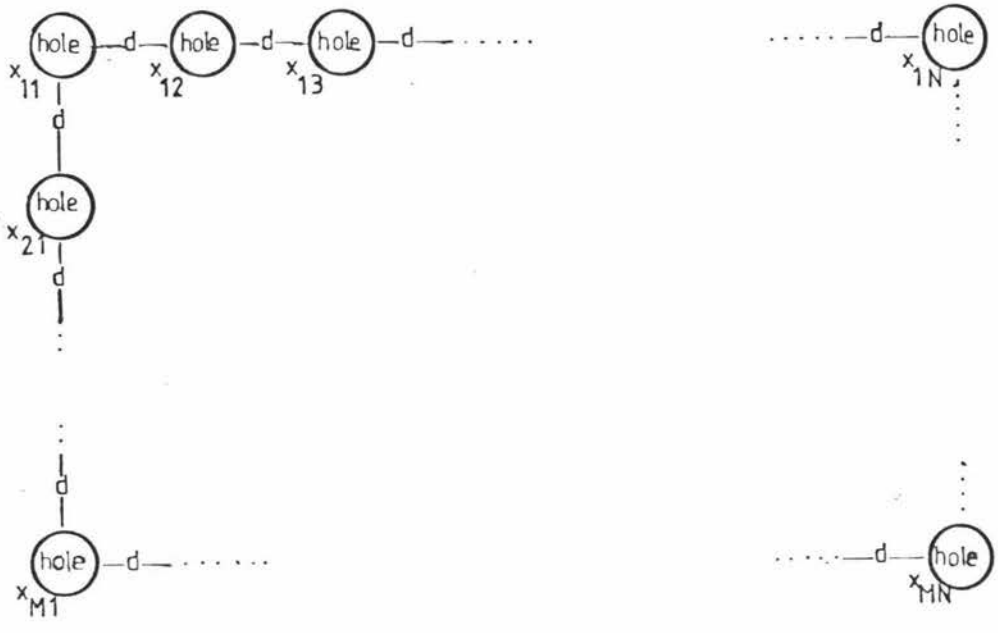

diagram 24

Total area = [(0.5+d) x N] x [(0.5+d) x M]

$$= MN\ (0.5 + d)^2$$

area of holes = $MN\ \pi \left(\frac{0.5}{2}\right)^2$

But 50% of the total area equals the area of the holes.

Therefore:

$$0.5\ MN\ (0.5 + d)^2 = MN\ \pi \left(\frac{0.5}{2}\right)^2$$

hence $d \simeq 0.1$ nm

When a PFO sample is cooled into a lamellar phase, without the presence of an external magnetic field, small randomly orientated crystallites of PFO occur. A minimum size of these crystallites is gauged from the observation of deuteron quadrupole splittings in such a sample (19). They must be greater than 2 nm in diameter for if they were smaller the deuteron quadrupole splittings would be averaged to zero. Thus the defects, large pores or cracks, can not be those between individual crystallites since it was shown above that for such a model diameters of $\sim$ 0.1 nm would be needed. The large pore model is inconsistent with the results (19).

Fundamental to the above conclusion is the estimation of the percentage of surface area in holes or cracks. This was deduced from the different anisotropies of diffusion of the lithium ion and water molecule as being a measure of the average hole/crack diameter. There is thought to be a high degree of counter ion binding occuring within this system (20). Such a binding would slow diffusion parallel to the bilayers and decrease the anisotropy. The anisotropy value of 1.92 may therefore be considered as a lower limit. From this additional consideration and the noticeably low anisotropy of water diffusion it is intuitively evident that a 50% estimate for the area of holes is not excessive.

The large pore model has also been considered to be inappropriate for biological lipid membranes, although a recent article supports the model (24). The reasons for discounting the large pore theory are:

(i) the high electrical resistance for the bilayers is considered incongruous (25).

(ii) since the self-diffusion for water should be proportional to the total area of the holes it is reasoned that the self-permeability determined from tracer experiments would be different to the self permeability determined by osmotic pressure, with the latter being considerably larger as a result of a hydrostatic pressure or osmotic gradient (22, 26-30). Recent work has determined the permeabilities to be equal (31-33).

(iii) Activation energies are always larger than 19 kJ/mole (15).

(iv) It is considered that no structural defects occur above

the temperature of the crystalline/liquid crystalline transition, and quite possibly that no defects occur below this temperature. Evidence for this comes from sonication of phospholipids (34).

Other models which have been proposed for passive transport of solvent across lipid membranes are:

(i) small pore
(ii) solubility-diffusion
(iii) energy barrier
(iv) thermal conformational disturbance

A brief description of each theory follows:

(i) small pore

In this model water is considered to pass through the membrane via pores which are small enough so that the water inside them does not exhibit bulk properties. Estimates of the activation energy range from 19 to 67 kJ/mole (15).

(ii) solubility-diffusion

This theory was first proposed by Zwolinski et al (8) and is given in terms of the Eyring absolute reaction rate theory (35). The membrane is assumed to be effectively a homogeneous layer in which water dissolves as discrete molecules and moves across by diffusion. The central idea of the theory is that the diffusion process consists of a series of molecular jumps and that the rate of jumping is constant. Price and Thompson have concluded that the activation energy would be between 44 and 52 kJ/mole for the rate limiting step occuring within the core of the bilayer (15). If the rate limiting step was diffusion through the bilayer/solution interface predictions were only that it would be larger.

(iii) energy barrier

This idea was first used by Langmuir and Schaeffer in reference to monolayer penetration by water and simple gas molecules at the air/water interface (36). Tien and Ting have considered this theory in conjunction with the theory proposed by Zwolinski et al and have postulated that water molecules cross membrane bilayers by 'barging' their way through, causing the creation of holes along the pathway as

the molecules permeate across (30). In terms of reaction rate theory only those water molecules striking the interfacial region with sufficient energy will get across the bilayer at the biface. The activation energy considered appropriate to the theory is about 28 kJ/mole. No activation is given for the case when the membrane interior is rate limiting since this possibility was discounted. Evidence for this was from observing the effects on permeation upon alteration of the ordered interfacial region (solution/membrane) by the introduction of ionic and neutral solutes. Also; from the addition of a certain proteinaceous material it was found that the dc resistance of the lipid membrane was lowered considerably while the permeability coefficient of water was little affected (37). It was therefore thought that ionic movement across the lipid membrane is governed by the nature of the membrane whereas water permeation is primarily determined by the orderliness of the interfacial region.

(iv) thermal conformational disturbance (38)

This is a theoretical model for transport of small neutral molecules, with an effective volume equal to or slightly larger than the volume of a CH_2 monomer, across membranes. The theory is concerned with thermal fluctuations in the hydrocarbon chains of the membrane lipids which cause conformational isomers of the hydrocarbon chains, or so called kink-isomers,to occur. Small molecules may enter the free volumes caused by such kinks and migrate across the membrane together with the kinks. The diffusion coefficient of kinks is calculated to be $10^{-9} m^2 s^{-1}$ and the activation energy of the process to be 20 kJ $mole^{-1}$. The hydrocarbon phase of the lipid membrane is considered as a defective ordered structure and so the model will not be applicable when the degree of disorder is so high that the hydrocarbon phase resembles a fluid more than an ordered structure.

In the literature there is a general disposition towards either the solubility-diffusion or activation energy barrier mechanisms, with perhaps opinion in favour of the solubility-diffusion process. The relevancy of a particular mechanism is often discussed in terms of the observed and predicted activation energies. However implicit within any such discussions concerning activation energies is the assumption that the composition and structure of the membrane do not change over the temperature range studied. If such a structural change occurs it may affect the diffusion activation energy of water movement across the membrane. This has previously been discounted since results for biological membranes using osmotic pressure, P_{os}, revealed a linear relationship between $\ln P_{os}$ and 1/T arguing against any abrupt change (14). It was considered that within the temperature range observed a sudden structure change would be due to a 'melting of the hydrocarbon chains' and would be shown as a discontinuity in permeability.

Examination of the results of the 46% and 52% by weight water samples (Figures 11 and 13) shows an abrupt and distinct discontinuing in the parallel diffusion measurements at the isotropic/nematic transition. No sharp discontinuities are observed within the lamellar region suggesting that no structural changes are occuring. A possible explanation of these lamellar phase results may be obtained by a comparison with results from studies of water diffusion in clay minerals by neutron spectroscopy (39). Water layers of reproducible thickness have been found to be producible between the aluminosilicate sheets of vermiculites and montmorillonite clay minerals. The measurements were confined to diffusive motions less than or of the order of the layer thickness, i.e. $\leq$ 0.5 nm. Results revealed a linear relationship between the logarithm of the diffusion rate perpendicular to the layers and the reciprocal of the distance between layers. Theory in explanation of these results was given by combining the Stokes-Einstein and Eyring theories for viscosity and diffusion (35) with the Kelvin equation (40) for the free energy of water in thin layers between curved surfaces.
The following relation was obtained

$$D = D_{Bulk} \quad \exp- \left[\frac{K}{dRT}\right]$$

where d is the water layer thickness and K is a constant.

The activation energy found from an Arrhenius plot will, therefore, be equal to K/dR. With respect to permeation mechanisms an important assumption so far has been that, for a given sample, the calculation of the activation energy is independent of processes other than the processes of permeation and viscous movement of water molecules. From Olejnik and White's work on clay minerals one may see that a layer width dependence upon temperature could be occuring, and in such a way as to lower the observed activation energy of permeation. Such a layer width dependence is a reasonable postulate since it has been shown that the water layer width varies upon alteration of weight fraction or upon the addition of a solvent such as octanol (23). Evidence for such a dependence is observed from examination of the D_{II} /temperature results of the 46% and 52% by weight water samples studied here. The activation energies for D_{II} are very small, much smaller than the free water value. The very small decrease in diffusion rate with decrease in temperature can be explained by the bilayers separating. As the bilayers separate more water moves in between lessening the effect the head groups have in restricting water movement parallel to the bilayers. If the volume of water between the bilayers increases, the water must be coming from the bilayer structure. This is plausible considering the extent of water permeation into hydrocarbon micelle interiors (41) and the liquid like nature of a liquid crystal. Such a trend would give a bilayer structure of variable PFO density. A representation of this trend is shown in diagram 25.

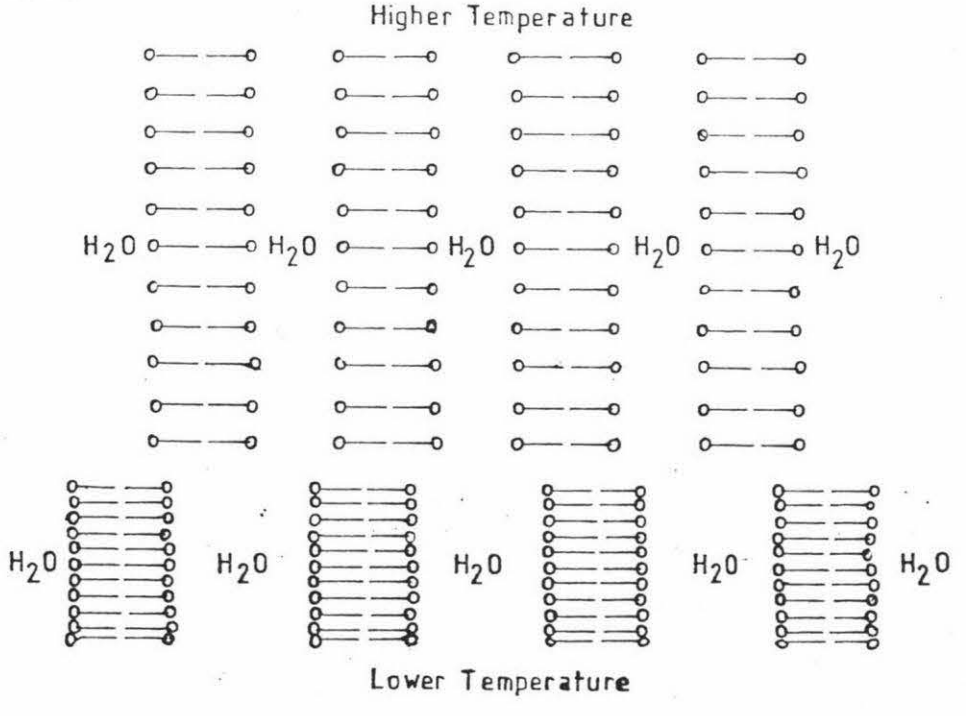

diagram 25

Due to the low anisotropy in diffusion parallel and perpendicular, diffusion willnot be strictly confined to such axis and so it may be necessary to consider water as having 3 dimensional diffusion properties but with obstructions greatest in the perpendicular direction. Even with this model diffusion parallel to the bilayers will still be facilitated as the distance between the bilayers increases.

As the fluorocarbon chains approach one another within a bilayer the diffusive movement of water across the bilayer will be effected. A closing of the chains would reduce the volume of the water within the actual bilayer reducing the rate of diffusion of water by a volume effect but also increasing the diffusion rate by reducing hydrogen bonding. The volume effect would be the more dominant. This, therefore, must exclude the small pore theory since a reduction in the core size would increase resistance to permeation causing a discontinuity in perpendicular diffusion rates at the isotropic/nematic, lamellar phase boundary.

The thermal conformation disturbance model is unlikely since, according to Trauble, such a mechanism is inapplicable when the degree of disorder is so high that the hydrocarbon phase (in this case fluorocarbon) resembles a fluid more than an ordered structure.

The activation energy barrier and solubility-diffusion mechanism are more difficult to interpret but in either case rate limiting diffusion steps within the interior of the bilayer would reflect in a similar discontinuity to the small pore theory. However for these mechanisms the possibility of a rate limiting step at the biface is shown by the lack of any large discontinuities in D_1 values over the thermotropic phase transitions. Over the diffusion distance measured along the perpendicular axis a water molecule would meet, on average, the same number of head groups irrespective of the phase and thus no permeation related discontinuity would be expected to be observed. Any slight discontinuity occuring may be due to the fact that water movement is effected by a transitory association of water and head groups since with the bilayers formed an associated water molecule would be stopped, lowering the diffusion rate, whereas in the isotropic phase the random movement of PFO chains ($5 \times 10^{-12} m^2 s^{-1}$ (19) at 315K) would not retard water diffusion as much.

More work must be carried out to achieve finer distinction between theories. In particular, it has been mentioned, in reference to lipid membranes, that a disturbance of the interfacial region may help distinguish between the activation energy barrier mechanism and the solubility - diffusion mechanism (15). Use may, perhaps, be made of Gurney's order/disorder concept of water (42). According to this concept water possesses distinctive structural features. Depending upon the size of ionic species introduced those ions which are most comparable in size to the structural vacancies of the water lattice will disrupt the lattice least. A typical disorder producing ion is given as Cs^+ and a typical order producing ion as Li^+ and, therefore, one may perhaps observe a difference in water diffusion between LiPFO and CsPFO.

CONCLUSION

The rigid impermeable bilayer model of the CsPFO lamellar phase is inconsistent with the water diffusion data. No restricted diffusion was observed across an experimental RMS distance of 6000 nm and there is only low anisotropy in the diffusion coefficients parallel and perpendicular to the surfactant bilayers. Attempts to explain the permeation of the bilayers in terms of the theories offered for passive diffusion across biological lipid membranes were generally unsuccessful. The large pore theory was discounted and the diffusion data was inconsistent with either the small pore or thermal conformational disturbance mechanisms. The attenuation in $D_\perp$ is so small that it could well be the result of hydration at the bilayer boundary and a small obstruction effect from the fluorocarbon chains.

This work suggests that there are sufficient structural differences between surfactants and lipid bilayers as to render the use of surfactant bilayers as models for transport across biological membranes unsatisfactory. In the surfactant system there is a distinct likelihood that it is the bilayer structural dependence on temperature which is the deciding factor in determining diffusion coefficient activation energies rather than the permeation mechanisms for transport across the bilayers.

APPENDIX 1

DIFFUSION RATES OF BINARY MIXTURES A COMPARISON BETWEEN FOURIER TRANSFORM AND ISOTOPIC METHODS

A.1.1 Introduction

The examination of the diffusivity of species within a binary mixture is of both practical and theoretical importance. From a theoretical point of view it is of importance in describing transport properties of fluid systems (43). There is also interest in the isotopic mass effect of self-diffusion (44).

The majority of diffusion studies have involved the use of diaphragm cells (45), optical methods (46), gel sectioning (44),or steady field gradient NMR using appropriately deuterated samples (47). The aim of this section was to illustrate the use of PFG FT NMR for such work and its advantages to using the isotopic PFG NMR method.

A.1.2 Experimental

Determination of the self-diffusion of both components of the benzene/methanol mixtures was by PFG FT NMR with integration of the appropriate signal peaks. The self-diffusion coefficient of methanol was also determined for methanol/benzene- D[6] mixtures.

The reagents used were benzene of analar grade and methanol of univar grade. The only additional purification of benzene was by molecular sieves. Methanol was purified by treatment with magnesium activated by iodine (48). The purification removes any water, since water is the main impurity, with dehydration being essentially due to the magnesium methylate formed. Samples were prepared gravimetrically.

The diffusion coefficients determined for methanol in methanol/ benzene-D[6] mixtures is in agreement with methanol diffusion coefficients in undeuterated samples. This is as expected and gives confidence in the technique.

A.1.3. Results and discussion

Diffusion coefficient data are shown tabulated in Table 9 and graphed in Figure 16

Diffusion measurements of methanol/benzene mixtures have been made by Ansari and Kratochwill by the use of deuterated samples and the steady gradient method (47). The results had a 10% error, which is far higher than with the technique used here, and significant differences in the trend in diffusion coefficients were observed. The results of this study differ from those of Ansari and Kratochwill in that here it is observed that benzene diffusion coefficients are higher at low benzene concentration and lower at high benzene concentrations, and that for methanol, diffusion coefficients are significantly larger at high and low methanol concentrations.

From the shpaes of the benzene and methanol diffusion coefficient/mole fraction curves it may be seen that self-association is the dominant interaction (47). This conclusion is supported by the existence of a positive enthalpy of mixing (0.67 kJ/mole) (49). The variation in diffusion coefficients must be as a result of a change in the average size of the associated species. There is a general agreement that the system is composed of a mixture of polymeric chains and rings of methanol but no consensus on the size or relative amounts of each (50). It is however thought from work using chemical shift data and IR spectroscopy that cyclic tetramers of methanol are a dominant component.

There must be competing interactions occuring within the system since the diffusion coefficient of methanol versus mole fraction curve goes through a minimum whereas the diffusion coefficient of benzene is approximately constant. At ~ 0.5 mole fraction the tendency of methanol to associate is at a maximum. This may well be due to benzene acting as directors to the methanol molecule since it has been shown that the interaction of the hydroxyl group with the π- electron system of benzene decreases on increasing dilution with benzene (47).

Further work on this system is required. In particular it would be of interest to study the region around 0.8 mole fraction methanol to determine if the very high diffusion coefficients for benzene and methanol are real. One of the main problems in the case where one of the components is in great excess is that with the low resolution probe used here the signal from the low concentration component tends to be superimposed on the wings of the very large excess component peak. This introduces a much greater uncertainty in the diffusion coefficients for these mixtures.

Since this work was completed a high resolution PFG probe has been developed which would enable accurate diffusion coefficients to be obtained in the limits where the concentration of either component tends to zero.

Diffusion coefficients of Methanol/Benzene mixtures

25°C

mole fraction methanol	$D/10^{-9}$ m^2 s^{-1}	
	methanol	benzene
1.000	2.53 (2)	
0.914	3.16 (8)	
0.888	2.4 (1)	2.81 (4)
0.803	2.25 (2)	2.54 (3)
0.777	2.65 (3)	2.62 (4)
0.762	2.22 (2)	2.44 (4)
0.682	2.09 (2)	2.49 (3)
0.662	2.18 (3)	2.45 (3)
0.604	2.19 (3)	2.43 (3)
0.568	2.03 (2)	2.40 (2)
0.482	2.19 (3)	2.44 (2)
0.397	1.96 (4)	2.28 (2)
0.346	2.05 (4)	2.42 (3)
0.327	2.18 (2)	2.49 (3)
0.220	2.40 (2)	2.06 (4)
		benzene - D[6]
0.711	2.10 (1)	
0.518	2.31 (8)	
0.399	2.09 (2)	
0.159	2.39 (3)	

Table 9

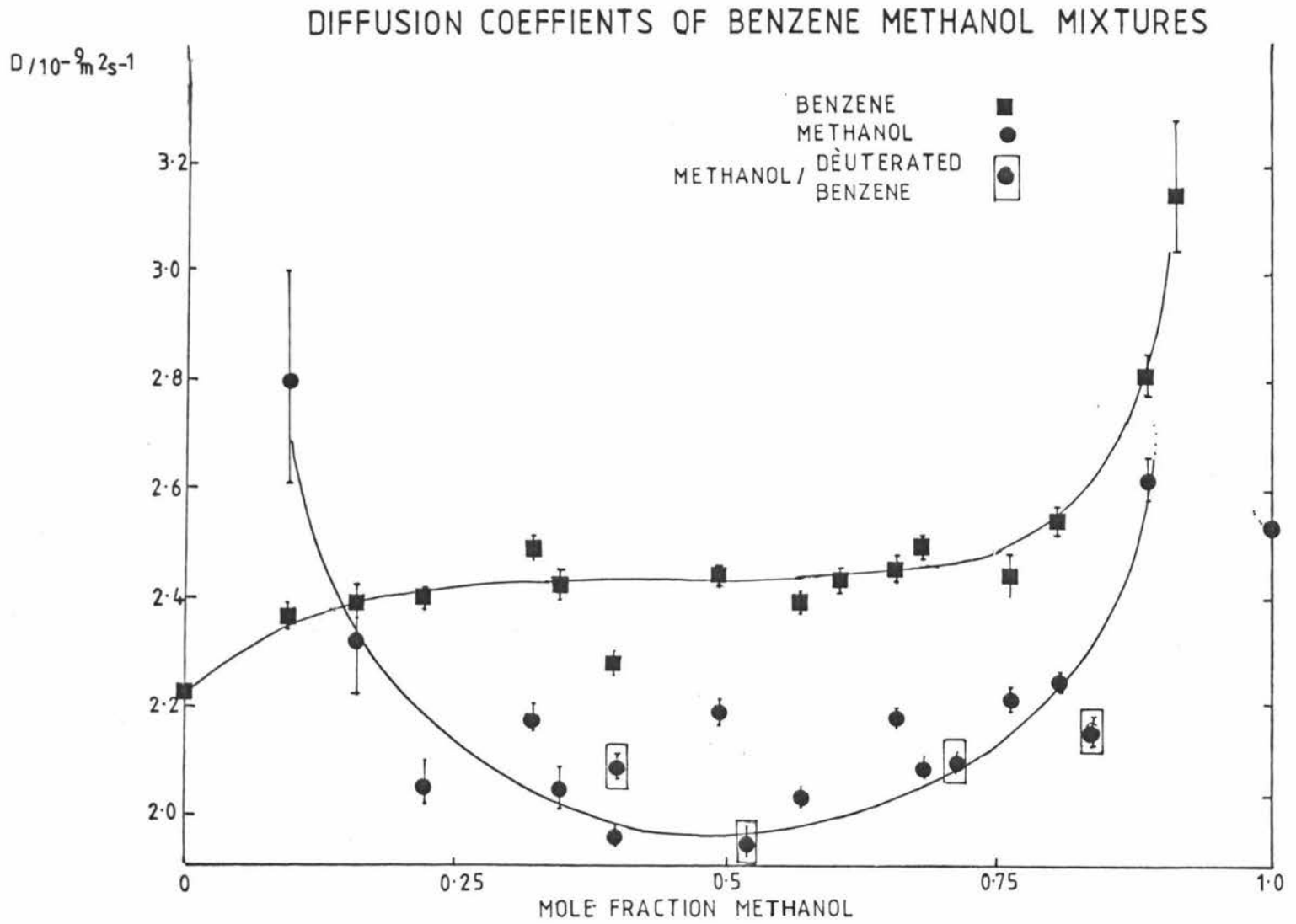
DIFFUSION COEFFIENTS OF BENZENE METHANOL MIXTURES
D /10⁻⁹m²s⁻¹
BENZENE
METHANOL
METHANOL / DEUTERATED BENZENE
3·2
3·0
2·8
2·6
2·4
2·2
2·0
0
0·25
0·5
0·75
1·0
MOLE FRACTION METHANOL

Figure 16

APPENDIX 2

The 74LS123N multivibrator features dc triggering from gated low-level-active (A) and high-level-active (B) inputs and also has overriding direct clear inputs. Complimentary outputs are provided. The overriding clear capability permits any output pulse to be terminated at a predetermined time independently of the timing components R and C. Diagram 26 illustrates triggering the one-shot with the high-level-active (B) inputs.

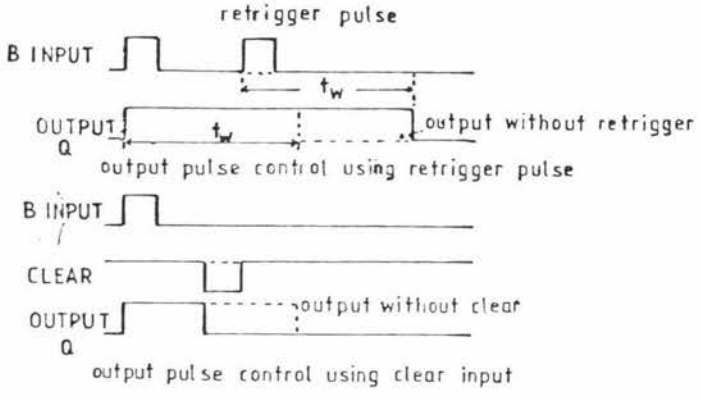

diagram 26

The truth table is shown.

inputs			outputs	
clear	A	B	Q	$\bar{Q}$
L	X	X	L	H
X	H	X	L	H
X	X	L	L	H
H	L	↑	⎍	⎎
H	↓	H	⎍	⎎
↑	L	H	⎍	⎎

⎍ = one high-level pulse
⎎ = one low-level pulse

The CD4017B is a 5 - stage Johnson counter having 10 decoded outputs and inputs which include a clock, a reset and a clock inhibit. The counter is advanced one count at the positive clock signal transition if the clock inhibit signal is low but not if the signal is high.

A high reset signal clears the counter to its zero count.

SN74LS123N

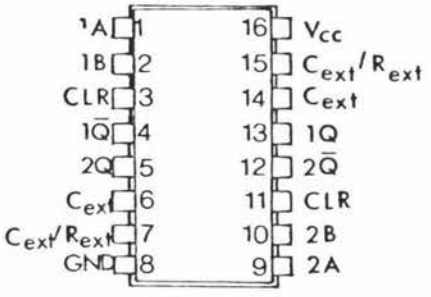

CD4017BC

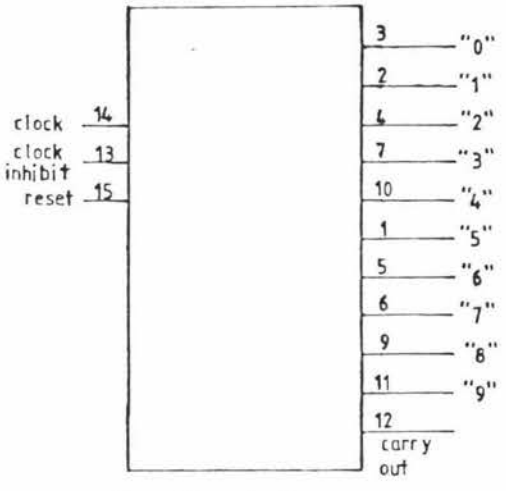

Functional diagram

BIBLIOGRAPHY

1. CARRINGTON, A. and A.D. McLachlan
Introduction to Magnetic resonance. Chapman and Hall Limited 1979.

2. EMSLEY, J.W., J.F eeney and L.H. Sutcliffe.
High resolution nuclear magnetic resonance spectroscopy. Pergamon Press Ltd., 1967.

3. FARRAR, T.C. and E.D. Becker
Pulse and Fourier transform NMR. New York and London Academic Press, 1971.

4. BLOCH, F
Nuclear induction. Physicol review 70: 460-474, 1946.
BLOCH, F.
The nuclear induction experiment. Physicol review 70: 474-485, 1946.

5. HAHN, E.L.
An accurate nuclear magnetic resonance method for measuring spin - lattice relaxation times. Physicol review 76: 145-146, 1949.

6. CARR, H.Y. and E.M. Purcell
Effects of diffusion on free precession in nuclear magnetic resonance experiments. Physicol review 94: 630-638, 1954.

7. MEIBOOM, S and D. Gill
Modified spin-echo method for measuring nuclear relaxation times. Review of scientific instruments 29: 688-691, 1958.

8. ZWOLINSKI, B.J., H. Eyring and C.E. Reese.
Diffusion and membrane permeability. Journal of physical chemistry 53: 1426-1452, 1949.

9. HARRIS, K.R., R. Mills, P.J. Back and D.S. Webster.
An improved NMR spin-echo apparatus for the measurement of self-diffusion coefficients: The diffusion of water in aqueous electrolyte solution. Journal of magnetic resonance 29: 473-482, 1978.

10. STEJSKAL, E.O. and J.E. Tanner
Spin diffusion measurements: Spin-echoes in the presence of

a time-dependent field gradient. Journal of chemical physics 42: 288-292, 1965.

11. CALLAGHAN, P.T., K.W. Jolley and J. Lelièvre. Diffusion of water in the endosperm tissue of wheat grains as studied by pulsed field gradient nuclear magnetic resonance. Journal of biophysics 28: 133-142, 1979.

12. WILLIAMS, W.D., E.F.W. Seymour and R.M. Cotts. A pulsed-gradient multiple spin-echo NMR technique for measuring diffusion in the presence of background magnetic field gradients. Journal of magnetic resonance 31: 271-282, 1978.

13. CALLAGHAN, P.T. , C.M. Trotter and K.W. Jolley. A pulsed field gradient system for a Fourier transform spectrometer. Journal of magnetic resonance 37: 247-259, (1980).

14. BANGHAM, A.D., M.M. Standish and J.C. Watkins. Diffusion of univalent ions across the lamellae of swollen phospholipids. Journal of molecular biology 13: 238-252,1965.

15. PRICE, H.D. and T.E. Thompson Properties of liquid bilayer membranes separating two aqueous phases: Temperature dependence of water. Journal of molecular biology 41: 443-457, 1969.

16. BEAR, R.S. , K.J. Palmer and F.O. Schmitt. X-ray diffraction studies of nerve lipids. Journal of cellular and comparative physiology 17: 355-367, 1941.

17. BODEN, N. , P.H. Jackson and K. McMullen. Are "nematic" amphiphilic liquid crystalline mesophases thermodynamically stable? Chemical physics letters 65: 476-479, 1979.

18. KHETRAPAL, C.L., A.C. Kunwar, A.S. Tracey and P Diehl. NMR studies in lyotropic liquid crystals, in: NMR - basic principles and progress, 9: Editors Diehl, P. , E. Fluck and R. Kosfeld. Springer, Berlin, 1975.

19. TIDDY, G.J.T. and E. Everiss
Self-diffusion in lyotropic liquid crystals measured by NMR, in: Magnetic resonance in interface science (ACS symposium series 34): Editors Reising, H.A. and C.G. Wade.

20. WANG, J.H.
Theory of the self-diffusion of water in protein solutions. A new method for studying the hydration and shape of protein molecules. Journal of the American chemical society 76: 4755-4763, 1954

21. CALLAGHAN, P.T., K.W.Jolley, J. Lelièvre and R.B.K. Wong.
NMR studies of wheat starch pastes.
Journal of colloid and interface science. In the press.

22. PAGANELLI, C.V. and A.K. Solomon. Rate of exchange of tritiated water across the human red cell membrane.
Journal of general physiology, 41: 259-277, 1957.

23. TIDDY, G.J.T., E. Everiss and B.A. Wheeler.
Phase diagram and NMR study of the lyotropic liquid crystalline phases formed by lithium perfluoro-octanoate and water.
Journal of the chemical society Faraday transactions I 72: 1747-1758, 1976.

24. FIFIELD, R.
Liposomes: bags of biological potential. New scientist 18: 150-153, 1980.

25. CASS, A and A. Finkelstein
Water permeability of thin lipid membranes. Journal of general physiology 50: 176 - 1784, 1967

26. RENKIN, E.M.
Filtration, diffusion, and molecular sieving through porous cellulose membranes. Journal of general physiology 38: 225-243, 1954.

27. PRESCOTT, D.M. and E. Zeuthen
Comparison of water diffusion and water filtration across cell surfaces. Acta physiologica Scandanavica 28: 77-94, 1953.

28. USSING, H.H.
In: Ion transport across membranes, pp. 3 - 22, editor H.T. Clarke, Academic Press, New York, 1954.

29. ROBBINS, E. and A.J. Mauro
Experimental study of the independence of diffusion and hydrodynamic permeability coefficients in colloidion membranes. Journal of general physiology 43: 523-532, 1960.

30. TIEN, H.T. and H.P. Ting
Permeation of water through bilayer lipid membranes. Journal of colloid and interface science 4: 702-713, 1968.

31. CASS, A and A.Finkeistein
Water permeability of thin lipid membranes. Journal of general physiology 50: 1765-1784, 1967.

32. FINKELSTEIN, A.
Effect of cholestrol on water permeability of thin lipid membranes. Nature 216: 717-718, 1967.

33. HANAI, T. , V.A. Haydon and W.R. Redwood.
The water permeability of artificial biomolecular leaflets: a comparison of radiotracer and osmotic methods. Annals of the New York academy of sciences 137: 731-739, 1966.

34. LAWACZECK, R.
On the permeability of water molecules across vesicular lipid bilayers. Journal of membrane biology 51: 229-261, 1979.

35. EYRING, H.
Viscosity, plasticity and diffusion as examples of absolute reaction rates. Journal of chemical physics 4: 283-291, 1936.

36. LANGMUIR, L. and V.J. Schaefer
Rates of evaporation of water through compressed monolayers on water. Journal of the Franklin institute 235: 119-162, 1943.

37. MUELLER, P., D.O. Rudin, H. Ti Tien and W.C. Wescott.
Formation and properties of biomolecular lipid membranes. In: Recent progress in surface science. Chapter 11. Editors Danielli, J.F., Pankhurst, K.G.A. and Riddiford, A.C. Academic Press, New York, 1964.

38. TRAUBLE, H.
The movement of molecules across lipid membranes: A molecular

theory. Journal of membrane biology 4: 193-208, 1971.

39. OLEJNIK, S. and J.W. White.
Think layers of water in vermiculites and montmorillonites - Modification of water diffusion. Nature physical science 236: 15-16, 1972.

40. ADAMSON, A.W.
Physical chemistry of surfaces. Wiley - Interscience, New York, 1967.

41. MENGER, F.M.
The water content of a micelle interior. Fjord versus reef models. Journal of the American chemical society 100: 4676 - 4678, 1978.

42. GURNEY, R.W.
Ionic processes in solution, chapters 3 and 16, McGraw-Hill, New York, 1953.

43. NAKANISHI, K
On the diffusivity on nonelectrolytes in infinitely dilute solution. Bulletin of the chemical society of Japan 51: 713-717, 1978.

44. FREER, R. and J.N. Sherwood
Diffusion in organic liquids. Part 2. Isotope mass effects in self-diffusion in benzene and cyclohexane. Journal of the chemical society, Faraday transactions I, 76: 1030-1037, 1980.

45. MILLS, R and L.A. Woolf
The diaphragm cell. Australian national university press, Canberra, 1968.

46. SHANKLAND, I.R., P.J. Dunlop and L.W. Barr.
Isotope-effect in liquids as shown by tracer diffusion at 25 degrees C of several labelled benzenes in benzene, chlorobenzene, N-octane, and cyclohexane, and relationship to the isotope-effect in solids. Physical review B- condensed matter 12: 2249-2252, 1975.

47. ANSARI, M.S. and A. Kratochwill
A nuclear magnetic relaxation study of the system benzene-

methanol. Journal of solution chemistry 7: 655-668, 1978.

48. VOGEL, A.I.
A text-book of practical organic chemistry, including qualitative analysis, 3rd ed., London, Longmans, Green and Co., 1956. 169p.

49. DANIELS, F and R.A. Alberty
Physical chemistry, 4th ed., Wiley, New York, 1975. Chapter 4.

50. INLOW, R.O., M.D. Joesten and J.R. Van Wazer.
Spin-lattice relaxation and hydrogen bonding in methanol-solvent mixtures. Journal of physical chemistry 79: 2307-2312, 1975.